

Semester Thesis

# Evaluation of the Applicability of Integrating Nephelometers in the Mie Regime

Spring Term 2024

**Supervised by:**  
Dr. Martin Gysel Beer  
Prof. Dr. Ulrike Lohmann

**Author:**  
Nicola Rupf



**Declaration of originality**

The signed declaration of originality is a component of every written paper or thesis authored during the course of studies. In consultation with the supervisor, one of the following three options must be selected:

- I confirm that I authored the work in question independently and in my own words, i.e. that no one helped me to author it. Suggestions from the supervisor regarding language and content are excepted. I used no generative artificial intelligence technologies<sup>1</sup>.
- I confirm that I authored the work in question independently and in my own words, i.e. that no one helped me to author it. Suggestions from the supervisor regarding language and content are excepted. I used and cited generative artificial intelligence technologies<sup>2</sup>.
- I confirm that I authored the work in question independently and in my own words, i.e. that no one helped me to author it. Suggestions from the supervisor regarding language and content are excepted. I used generative artificial intelligence technologies<sup>3</sup>. In consultation with the supervisor, I did not cite them.

**Title of paper or thesis:**

Evaluation of the Applicability of Integrating Nephelometers in the Mie Regime

**Authored by:**

*If the work was compiled in a group, the names of all authors are required.*

**Last name(s):**

Rupp

**First name(s):**

Nicola

With my signature I confirm the following:

- I have adhered to the rules set out in the Citation Guide.
- I have documented all methods, data and processes truthfully and fully.
- I have mentioned all persons who were significant facilitators of the work.

I am aware that the work may be screened electronically for originality.

**Place, date**

Zürich, 02.07.2024

**Signature(s)**

*N. Rupp*

<sup>1</sup> E.g. ChatGPT, DALL-E 2, Google Bard  
<sup>2</sup> E.g. ChatGPT, DALL-E 2, Google Bard  
<sup>3</sup> E.g. ChatGPT, DALL-E 2, Google Bard

*If the work was compiled in a group, the names of all authors are required. Through their signatures they vouch jointly for the entire content of the written work.*

# Contents

<b>Preface</b>	<b>vii</b>
<b>Abstract</b>	<b>ix</b>
<b>Symbols</b>	<b>xi</b>
<b>1 Theoretical Background</b>	<b>1</b>
1.1 Scattering of Light . . . . .	1
1.1.1 Light as a Plane Wave and Monochromaticity . . . . .	1
1.1.2 A Single Particle Scattering Quasi-Monochromatic Radiation	2
1.1.3 Independent Scattering by Many Particles . . . . .	5
1.1.4 Hemispherical Scattering . . . . .	5
1.1.5 Simplifications Due to Symmetries and Sample Properties . .	5
1.1.6 Mie's Solution and Scattering in Different Regimes . . . . .	6
1.2 Nephelometers . . . . .	8
1.2.1 Nephelometer Calibration in the Rayleigh Regime and Relation between Theoretical and Measured Scattering Coefficients	9
1.2.2 The Illumination Function . . . . .	11
1.3 Particle Distributions . . . . .	12
1.3.1 Normal Distribution . . . . .	12
1.3.2 Lognormal Distribution . . . . .	12
1.3.3 Scattering Coefficients of Particle Distribution . . . . .	13
<b>2 Methods</b>	<b>15</b>
2.1 Work with Nephelometers . . . . .	15
2.1.1 Nephelometers Used and Their Mode of Operation . . . . .	15
2.1.2 Instrument Calibration . . . . .	16
2.1.3 Illumination Functions of the Nephelometers . . . . .	16
2.2 DEHS Scattering . . . . .	18
2.2.1 General Properties of DEHS . . . . .	19
2.2.2 DEHS' Refractive Index . . . . .	19
2.2.3 Experimental Setup . . . . .	19
2.2.4 Calculation of Expected Scattering Coefficients . . . . .	20
<b>3 Results and Discussion</b>	<b>21</b>
3.1 Instrument Calibration . . . . .	21
3.2 Illumination Functions of the Nephelometers . . . . .	21
3.2.1 Illumination Function of NE300 . . . . .	21
3.2.2 Illumination Function of IN101 . . . . .	22
3.3 DEHS Scattering . . . . .	23
3.3.1 Refractive Index of DEHS . . . . .	23
3.3.2 Particle Size Distribution . . . . .	24

3.3.3	Measured and Corrected Scattering Coefficients . . . . .	25
<b>4</b>	<b>Conclusion</b>	<b>29</b>
	<b>Bibliography</b>	<b>31</b>
<b>A</b>	<b>Figures</b>	<b>33</b>
A.1	Illumination Functions . . . . .	33
A.1.1	Illumination Functions of NE300 . . . . .	33
A.1.2	Illumination Functions of IN101 . . . . .	35

# List of Figures

1.1	A linearly polarized plane wave [1] . . . . .	2
1.2	A plane wave incident on a particle. Scattering as a spherical wave, at far enough distances it can be approximated as a plane wave again.	2
1.3	How I (and other authors) choose to describe the scattering of an incoming plane wave with wave vector $\mathbf{k}^0$ at the origin, being measured as a plane wave with wave vector $\mathbf{k}$ afterwards (compare e.g. [2],[3]) The light blue plane spanned by $\mathbf{k}^0, \mathbf{k}$ is the scattering plane. We describe the situation in spherical coordinates, using the <i>polar angle</i> $\theta$ and <i>azimuthal angle</i> $\varphi$ . . . . .	3
2.1	The light path of the NE300 nephelometer during hemispherical back scattering. Directly taken from the manual[4] . . . . .	15
2.2	Relative signal vs. angle for the different wavelengths and detector regions (front scattering and back scattering) of IN101, provided by AirPhoton. Note that the angle is given as the difference from $0^\circ$ for hemispherical front scattering and $180^\circ$ for hemispherical back scattering. . . . .	17
2.3	The combined ansatz for the illumination function of the IN101 with optimized parameters . . . . .	18
2.4	The setup for measuring the scattering coefficients of different log-normal size distributions of DEHS . . . . .	20
3.1	The relative signal and respective fits for the NE300, both full and hemispherical back scattering ranges are shown for NE300's wavelengths 635 nm (red), 525 nm (green) and 450 nm (blue). The axis orientation was chosen to be consistent with the angle conventions from Figure 1.3. . . . .	22
3.2	The relative signal and respective fits for the IN101, both full and hemispherical back scattering ranges are shown for IN101's wavelengths 632 nm (red), 532 nm (green) and 450 nm (blue). As in Figure 3.1, I choose to mirror the x-axis, such that the measurements of the back scattering detector ( $\triangleleft$ , left part of the plot) and front scattering detector ( $\triangleright$ , right part of the plot) match the coordinate conventions from Figure 1.3. . . . .	23
3.3	The literature values[5][6] of the refractive index of DEHS (compare Table 2.1) along with an inversely proportional fit (see Equation 2.9)	24
3.4	Scatter plot of mean midpoint diameter distributions for two particle size ranges, about 300 nm and about 600 nm. Additionally, a (not normalized) lognormal in spacing $dN/d\log_{10} D_p$ fit is performed on each distribution, as described in Equation 1.65 . . . . .	24

3.5	Measured versus corrected (independent scattering coefficients adjusted for illumination function effect) full scattering coefficients for both nephelometers. The data of IN101 of the size distribution with a geometric mean of 594.7 nm has been omitted due to saturation. The dashed line indicates the position of perfect agreement. . . . .	26
3.6	Measured versus corrected (independent scattering coefficients adjusted for illumination function effect) hemispherical back scattering coefficients for both nephelometers. The dashed line indicates the position of perfect agreement. . . . .	26
3.7	Ratios of measured to independent (i.e. expected, so corrected for illumination function and calibration: Firstly hemispherical back scattering ratios and secondly spectral ratios of full scattering coefficients. The smaller markers are indicating a geometric mean size of 313.5 nm, the larger ones a geometric mean size of 797.4 nm. The colors of the back scattering fractions correspond to the illuminating wavelength of the respective nephelometer. The x coordinate of a given ratio of full scattering spectral ratios is chosen as the mean corrected scattering coefficient of the two illuminating wavelengths of the respective colors. . . . .	27
A.1	NE300's full and hemispherical back scattering illumination function for an illuminating wavelength of 450 nm . . . . .	33
A.2	NE300's full and hemispherical back scattering illumination function for an illuminating wavelength of 525 nm . . . . .	34
A.3	NE300's full and hemispherical back scattering illumination function for an illuminating wavelength of 635 nm . . . . .	34
A.4	IN101's full and hemispherical back scattering illumination function for an illuminating wavelength of 450 nm . . . . .	35
A.5	IN101's full and hemispherical back scattering illumination function for an illuminating wavelength of 532 nm . . . . .	35
A.6	IN101's full and hemispherical back scattering illumination function for an illuminating wavelength of 632 nm . . . . .	36

# List of Tables

2.1	Literature values for the refractive index of DEHS at different wavelengths, obtained from [5][6] . . . . .	19
3.1	Calibration coefficients $c_{0, \text{ang. width}}^{\text{IN100}, \lambda}$ , $c_{1, \text{ang. width}}^{\text{IN100}, \lambda}$ for IN101 . . . . .	21
3.2	Calibration coefficients $c_{0, \text{ang. width}}^{\text{NE300}, \lambda}$ , $c_{1, \text{ang. width}}^{\text{NE300}, \lambda}$ for NE300 . . . . .	21
3.3	Minimized sum of least squares residuals and respective ratio to blue (450 nm) forward scattering. 'bw' stands for hemispherical back scattering and 'fw' stands for hemispherical forward scattering. . . . .	22
3.4	The different scattering types' optimized parameters for our model of IN101's illumination function (see Equation 2.8) . . . . .	23
3.5	Measured and independent scattering coefficients adjusted for illumination function effect (i.e. expected scattering coefficients) ( $\text{Mm}^{-1}$ ) of the size distribution with a geometric mean of 313.5 nm. The expected values of IN101 and NE300 differ due to the different illuminating wavelengths and illumination functions of the nephelometers. . . . .	25
3.6	Measured and independent scattering coefficients adjusted for illumination function effect (i.e. expected scattering coefficients) ( $\text{Mm}^{-1}$ ) of the size distribution with a geometric mean of 594.7 nm. The expected values of IN101 and NE300 differ due to the different illuminating wavelengths and illumination functions of the nephelometers. . . . .	25
3.7	Measured and expected hemispherical back scattering fraction $\beta$ for the size distribution with a geometric mean of 313.5 nm . . . . .	27
3.8	Measured and expected hemispherical back scattering fraction $\beta$ for the size distribution with a geometric mean of 594.7 nm . . . . .	27

# Acknowledgements and use of generative AI

## Personal Acknowledgements

I thank the Aerosol Physics and Optics group at PSI's Laboratory of Atmospheric Chemistry for offering me the opportunity to explore this field, and for their support and assistance during the entire project, especially Dr. Martin Gysel Beer and 许启之 (QiZhi Xu). Furthermore, I thank Prof. Dr. Ulrike Lohmann for her readiness to supervise this project.

## Use of Generative Artificial Intelligence

I used the free version of ChatGPT for tasks involving programming, especially for debugging, generating plots and LaTeX tables and learning how to handle the *pandas* package's data frames. Being somewhat aware of how ChatGPT is trained, I, to my best knowledge and judgement, did not use any generated responses where I would have believed citations to be necessary or adequate.



# Abstract

Nephelometers are calibrated using small particles, often gas molecules. They are then utilized to measure the scattering of light off different substances which can be orders of magnitude larger than the Angstrom-range gases. This discrepancy of calibrating and measuring in different relative size regimes can cause measurements to deviate from theoretical predictions. Compactly introducing scattering theory's basics in the first chapter, including Mie's solution, I determine calibration coefficients for two integrating nephelometers, Acoem Australasia's Aurora NE-300 and AirPhoton's IN101, for full scattering and hemispherical back scattering at three different wavelengths each, which allows transforming signals into scattering coefficients. Furthermore, I characterize the nephelometers' measuring properties by giving parameters to analytical illumination functions for the IN101 and providing accurate and reproducible fits for NE300's illumination function. For two quasi-monodisperse samples of spherical di-ethylhexyl-sebacat (DEHS) with median particle diameters of 313.5 nm and 594.7 nm, respectively, I calculate, using interpolated instead of analytical illumination functions to reduce uncertainty, expected absolute values of scattering coefficients and compare to the ones measured by IN101 and NE300. The expected values are the theoretical values adapted to the respective nephelometer's illumination and calibration characteristics. IN101 is saturated for full scattering of the size distribution with a larger median diameter, where NE300 generally provides more accurate results. For the other size distribution however, IN101's values better coincide with the expected ones. IN101 generally underestimates scattering coefficients, while NE300 consistently overestimates them. I assess internal nephelometer consistency in two ways. Firstly, by taking the ratio of measured and expected hemispherical back scattering fractions. Secondly by assessing the spectral consistency of measured full scattering coefficients. Here measured ratios of different pairs of illuminating wavelengths are compared to their expected counterparts. The ratios of hemispherical back scattering fractions are unsatisfactory, especially for NE300. Only one of six values lies within the desired 10 %. However, a real comparison to IN101 requires more valid data points. This results needs further investigation, as the reason is unknown. Contrarily, all values describing spectral consistency are within 8.2 % of unity, the ones from the size distribution with a median diameter of 313.5 nm being even more accurate for both instruments. For future work I suggest that firstly, more data points are assessed and secondly, the two parameters *median size* and *particle concentration* are varied independently, thus allowing to not only detect patterns and limits of nephelometer performance, but also their respective origins.



# Symbols

## Acronyms

AAC	Aerodynamic aerosol classifier
CPC	Condensation particle counter
DEHS	Di-ethylhexyl-sebacat
HEPA	High efficiency particulate air
Laser	Light Amplification by Stimulated Emission of Radiation
LED	Light emitting diode
MFC	Mass flow controller
PDF	Probability distribution function
PMT	Photomultiplier tube
RHS	Right hand side
SEM	Standard error of the mean
SMPS	Scanning mobility particle sizer
STD	Standard deviation
STP	Standard temperature and pressure



# Chapter 1

## Theoretical Background

### 1.1 Scattering of Light

In the context of this thesis, scattering describes the collision or interaction of electromagnetic radiation with a particle. The electromagnetic radiation relevant for the experiment lies within the visible spectrum so we use the terms electromagnetic radiation and light interchangeably.

In the following we will provide a short introduction to the scattering of light off of particles. Some excellent and thorough books on the matter are Craig F. Bohren and Donald R. Huffman's *Absorption and Scattering of Light by Small Particles* ([2]), J. W. Hovenier, C. van der Mee and H. Domke's *Transfer of Polarized Light in Planetary Atmospheres* ([3]) and James E. Hansen and Larry D. Travis' *Light Scattering in Planetary Atmospheres* ([8]), which have proven to be a great help. Most theory shown here is their work.

#### 1.1.1 Light as a Plane Wave and Monochromaticity

The nephelometers implemented for the experiments in this report use approximately monochromatic LEDs (Light emitting diodes) to measure particles' characteristics, which are far away compared to the particles' dimensions. Therefore, one suitable approach to describe the incoming electromagnetic radiation is a plane wave.

The amplitude of an along  $\frac{A}{\lambda}$  linearly polarized plane wave with wave vector  $\mathbf{k} = \frac{2\pi}{\lambda} \mathbf{e}_k$  has the shape

$$\mathbf{A}(x, t) = A_0 e^{i(\mathbf{k} \cdot \mathbf{x} - \omega_{|\mathbf{k}|} t)} \quad (1.1)$$

where  $\mathbf{e}_k$  points into the direction of propagation and  $\lambda$  is the wavelength. With the velocity of the wave in the medium  $c_n$  we also get the angular frequency  $\omega_{|\mathbf{k}|} = |\mathbf{k}| \cdot c_n$ .

Unlike the linearly polarized radiation depicted in Figure 1.1, unpolarized electromagnetic radiation does not posses a regular shape. Instead, it can be thought of as a superposition of enough polarized radiation for a polarization measurement yielding a completely random result. Note, however, that unpolarized radiation can still be monochromatic.

Regarding monochromaticity, we remark that no continuous source of electromagnetic radiation, not a LED or even a laser, is completely monochromatic. For our purposes, the sources' bandwidths (the widths of the wavelength or frequency spectra of the emitted radiation) are small and symmetric enough for me to approximate them as consisting of only a single wavelength, for which producers report the wavelength in the center of the distribution.

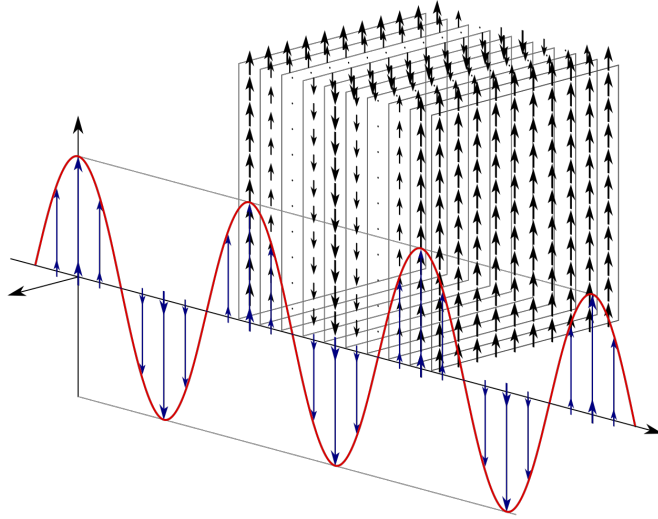


Figure 1.1: A linearly polarized plane wave [1]

### 1.1.2 A Single Particle Scattering Quasi-Monochromatic Radiation

We begin by considering a plane wave propagating along the positive z-axis, which is incident on a particle residing at the origin. For large distances from the origin ( $|\mathbf{x}| \gg d, \lambda$ , the so called *far field approximation*), the solution to the inhomogeneous Maxwell Equations is locally a plane wave propagating in direction of the position of interest, where the measurement is conducted[9].

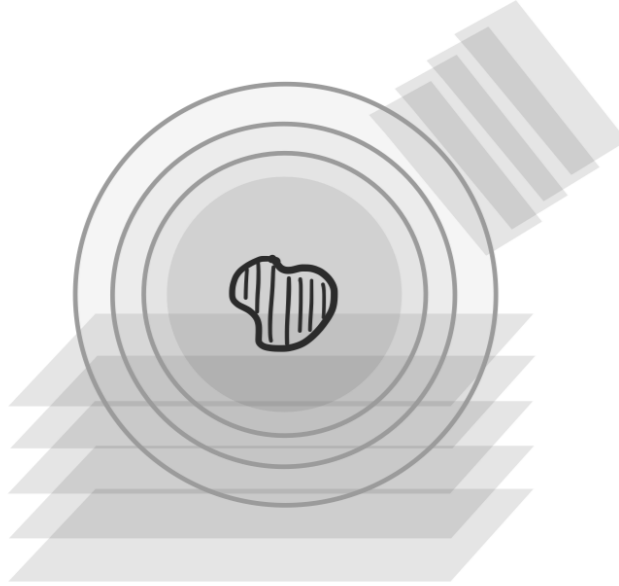


Figure 1.2: A plane wave incident on a particle. Scattering as a spherical wave, at far enough distances it can be approximated as a plane wave again.

In the following we proceed similarly to Hovenier et al.([3]). The plane spanned by the wave vectors of the incident wave ( $\mathbf{k}^0$ ) and the scattered wave ( $\mathbf{k}$ ) is called the *scattering plane*. For both waves we choose to write their electric field in a basis of

two unit vectors  $\mathbf{r}^0, \mathbf{l}^0$  and  $\mathbf{r}, \mathbf{l}$  respectively. We define  $\mathbf{r}^0, \mathbf{r}$  to be orthogonal to the scattering plane and  $\mathbf{l}^0, \mathbf{l}$  to be parallel to the scattering plane, such that  $\mathbf{r}^0, \mathbf{l}^0, \mathbf{k}^0$  and  $\mathbf{r}, \mathbf{l}, \mathbf{k}$  each form a right-handed orthogonal basis of  $\mathbb{R}^3$ .

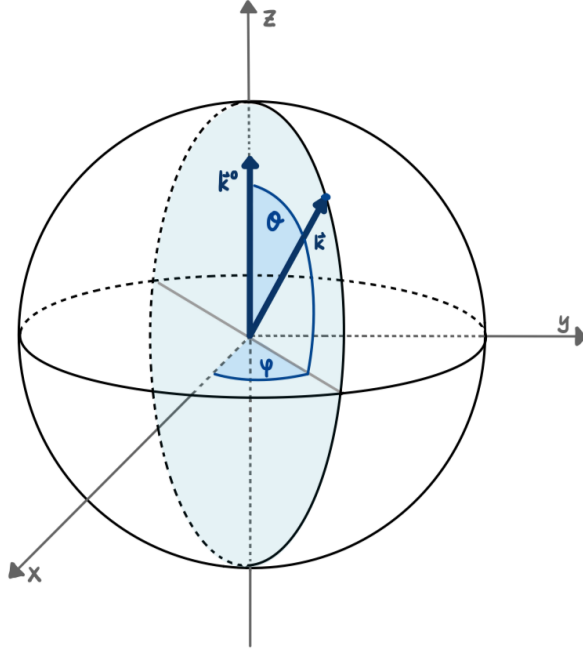


Figure 1.3: How I (and other authors) choose to describe the scattering of an incoming plane wave with wave vector  $\mathbf{k}^0$  at the origin, being measured as a plane wave with wave vector  $\mathbf{k}$  afterwards (compare e.g. [2],[3]) The light blue plane spanned by  $\mathbf{k}^0, \mathbf{k}$  is the scattering plane. We describe the situation in spherical coordinates, using the *polar angle*  $\theta$  and *azimuthal angle*  $\varphi$ .

The respective electric fields can then be rewritten as [3]

$$\begin{pmatrix} E_l^0 \\ E_r^0 \end{pmatrix} = e^{-ikz+i\omega t} \begin{pmatrix} a_l^0 \exp(-i\varepsilon_1^0) \\ a_r^0 \exp(-i\varepsilon_2^0) \end{pmatrix} \quad (1.2)$$

and

$$\begin{pmatrix} E_l \\ E_r \end{pmatrix} = \frac{e^{-ikR+ikz}}{ikR} \mathbf{S}(\theta, \varphi) \begin{pmatrix} E_l^0 \\ E_r^0 \end{pmatrix} \quad (1.3)$$

which in turn defines a *scattering matrix*, using Hovenier et al.'s notation ([3])

$$\mathbf{S}(\theta, \varphi) = \begin{pmatrix} S_2(\theta, \varphi) & S_3(\theta, \varphi) \\ S_4(\theta, \varphi) & S_1(\theta, \varphi) \end{pmatrix} \quad (1.4)$$

Note that the different sign in the plane wave is not physically relevant, as  $\text{Re}(\exp(i\alpha)) = \text{Re}(\exp(-i\alpha))$ .

We will now take a short detour from the usual pathway of describing scattering by a single particle, sparing us from introducing many new concepts which are irrelevant for the unpolarized case we are considering.

We define the *scattering cross section*  $\sigma_{\text{sca}}$  as a single particle as the ratio between

- the time average of the total energy radiated by the particle, per unit time (dimension: energy / time)

- the time average energy of the incident plane wave per unit time per unit area (dimension: energy / (time · area))

which results in  $\sigma_{\text{sca}}$  being an area. We can motivate this definition by arguing, that we are not interested in any information regarding the size of the particle, only in how it scatters an incoming field.

We define a *flux*  $\Phi$  as an energy flow in a given direction per unit time per unit area. Using that the energy density of a plane electromagnetic wave is  $|\mathbf{E}|^2$ [9] and remembering  $\mathbf{E}_r^0 \perp \mathbf{E}_l^0$  and  $\mathbf{E}_r \perp \mathbf{E}_l$ , we derive that for these monochromatic plane waves

$$\Phi^0 = c(|\mathbf{E}_r^0|^2 + |\mathbf{E}_l^0|^2) \mathbf{e}_{\mathbf{k}^0} \quad (1.5)$$

and

$$\Phi = c(|\mathbf{E}_r|^2 + |\mathbf{E}_l|^2) \mathbf{e}_{\mathbf{k}} \quad (1.6)$$

Because in the experiment we are dealing with quasi-monochromatic waves, we take a time average over a time span large compared to the individual oscillation periods and get, applying  $\langle \cos^2(\omega t) \rangle = \langle \sin^2(\omega t) \rangle = 1/2$

$$\langle \Phi^0 \rangle = \frac{c}{2} (\langle |\mathbf{E}_r^0| \rangle^2 + \langle |\mathbf{E}_l^0| \rangle^2) \mathbf{e}_{\mathbf{k}^0} \quad (1.7)$$

and

$$\langle \Phi \rangle = \frac{c}{2} (\langle |\mathbf{E}_r| \rangle^2 + \langle |\mathbf{E}_l| \rangle^2) \mathbf{e}_{\mathbf{k}} \quad (1.8)$$

The time average total scattered energy per unit time is then given by integrating the flux over sphere of radius  $R$ , which is the distance of the detector from the source. Switching from Cartesian to Spherical coordinates gives ( $dx dy dz \rightarrow r^2 dr \sin \theta d\theta d\varphi$ ,  $r \equiv R$ )

$$R^2 \int_0^{2\pi} \int_0^\pi \langle \Phi(\theta, \varphi) \rangle \sin(\theta) d\theta d\varphi \quad (1.9)$$

and the time average energy of the incident plane wave per unit time per unit area is given by exactly by the flux  $\langle \Phi^0 \rangle$ . Dividing Equation 1.9 by the incoming flux, we get the scattering cross section of the particle  $\sigma_{\text{sca}}$ . Note that the hard part remains, we haven't solved for  $\mathbf{S}(\theta, \varphi)$ .

There is also a more compact, but somehow more abstract way to arrive at the above result. We define the *phase function*  $F_{11}(\theta, \varphi)$  by the following relation

$$\langle \Phi(\theta, \varphi) \rangle = \frac{1}{k^2 R^2} F_{11}(\theta, \varphi) \langle \Phi^0 \rangle \quad (1.10)$$

Inserting into Equation 1.9 yields

$$\sigma_{\text{sca}} = \frac{1}{k^2} \int_0^{2\pi} \int_0^\pi F_{11}(\theta, \varphi) \sin(\theta) d\theta d\varphi \quad (1.11)$$

Note, that we still have not solved for the relationship between the incoming and outgoing radiation, described by  $\mathbf{S}(\theta, \varphi)$  or equivalently  $F_{11}(\theta, \varphi)$ .

The above procedure is universally valid. However, generally not only total scattering intensities are of interest, but also how incoming and outgoing waves are polarized. We could therefore extend the above formalism and describe polarization using *Stokes vectors*, extending  $F_{11}(\theta, \varphi)$  to *transformation matrices* and use different clever bases. All this is excellently described in the books mentioned above ([2],[3],[8]) and many more, but exceeds the needs of the following experiments and therefore scope of this project.

One quantity we will use however is the *scattering efficiency*  $Q_{\text{sca}}$ , which can be defined from the scattering cross section as

$$Q_{\text{sca}} = \frac{\sigma_{\text{sca}}}{\pi r^2} \quad (1.12)$$

, where  $r$  is the radius of the particle. Notice that for non-spherical particles it might not be straightforward to define a radius. In this case the radius is substituted with a general characteristic dimension of the particle.

### 1.1.3 Independent Scattering by Many Particles

Consider some collection of, without loss of generality, different particles. Making the following assumptions for scattering by an incoming, quasi-monochromatic plane wave (both [3]):

- Each particle only scatters incoming radiation once
- The entire collection is centered at the origin

We then have[3], analogously to Equation 1.10,

$$\langle \Phi(\theta, \varphi) \rangle = \frac{\langle \Phi^0 \rangle}{k^2 R^2} \sum_{g \in \text{collection}} F_{11}^g(\theta, \varphi) \quad (1.13)$$

where the sum of all phase functions is noted as

$$F_{11}^C(\theta, \varphi) := \sum_{g \in \text{collection}} F_{11}^g(\theta, \varphi) \quad (1.14)$$

A related but not equal expression is the phase function per unit volume of such collection, denoted as  $F_{11}^{cv}$ . If the context is clear, we will also denote  $F_{11}^{cv}$  as  $F_{11}$  for the sake of readability.

Similarly to the scattering cross section  $\sigma_{\text{sca}}$ , we define the *scattering coefficient*  $b_{\text{sca}}$  of such a collection as (following [3])

$$b_{\text{sca}} = \frac{1}{k^2} \int_0^{2\pi} \int_0^\pi F_{11}^{cv}(\theta, \varphi) \sin \theta d\theta d\varphi = n \overline{\sigma_{\text{sca}}} \quad (1.15)$$

where  $n$  is the particle density, the number of particles per unit volume, and  $\overline{\sigma_{\text{sca}}}$  is defined as the average scattering cross section.  $b_{\text{sca}}$  has dimensions of inverse length.

### 1.1.4 Hemispherical Scattering

If we only want to know how much a particle reflects, we integrate over the hemisphere with polar angles  $\theta \geq \pi/2$  instead of the entire unit sphere  $S^2$ . This is called *hemispherical back scattering*. Similarly, we define *hemispherical forward scattering* when only interested in polar angles  $\theta \leq \pi/2$ . For both cases, everything is analogous to full scattering and we have the equivalent definitions.

The *hemispherical back scattering fraction*  $\beta$  is the ratio between hemispherical back scattering coefficient  $b_{\text{bsca}}$  and full scattering coefficient  $b_{\text{sca}}$ [10]

$$\beta = \frac{b_{\text{bsca}}}{b_{\text{sca}}} \quad (1.16)$$

### 1.1.5 Simplifications Due to Symmetries and Sample Properties

In the following we will not be able to derive successive steps, as they get much more involving and mathematical than the physical description. Even general calculations on scattering off of spherically symmetric and homogeneous particles are not easy.

Nowadays mainly attributed to Gustav Mie's famous 1908 paper (see [7]), Bohren and Huffman lead through the problem (see [2]) and accompany it by comments such as "*the reader who has painstakingly followed the derivation of (4.37), and thereby acquired virtue through suffering*"[2]. We will not acquire virtue, instead citing results relevant to us and refer to the sources for further details.

Consider first a spherically symmetric particle made from an isotropic material, to which we will refer as *sphere* from now on. Bohren and Huffman explicitly solve the problem only for incident radiation linearly polarized along the x-axis, but due to above conditions, this also provides the solution for any other linear polarization[2] and thereby for any polarization, because linearly independent linear polarizations form a basis of all polarization states. Assuming the particles having no surface charge, it follows from Maxwell's equations boundary conditions[3], for example derived from the integral forms of Maxwell's equations[11], together with symmetries of a sphere, that  $\mathbf{E}_l, \mathbf{E}_r$  are proportional to  $\mathbf{E}_l^0, \mathbf{E}_r^0$ , respectively[2]. This implies  $S_3 = S_4 \equiv 0$ .

Assuming that the expansion in spherical harmonics uniformly converges, Bohren and Huffman show that for  $k \cdot r$  large enough[2],

$$\mathbf{E}_l \sim E^0 \frac{e^{ikr}}{-ikr} \cos \varphi S_2(\cos \theta) \quad (1.17)$$

$$\mathbf{E}_r \sim -E^0 \frac{e^{ikr}}{-ikr} \sin \varphi S_1(\cos \theta) \quad (1.18)$$

Especially,  $S_1, S_2$  are independent of the azimuthal angle  $\varphi$ .

In summary, the scattering matrix at large enough distances for spheres with no surface charge is of the simpler shape

$$S(\theta) = \begin{pmatrix} S_2(\theta) & 0 \\ 0 & S_1(\theta) \end{pmatrix} \quad (1.19)$$

leading the phase function to take on the form[8]

$$F_{11}(\theta) = \frac{1}{2}(S_2 S_2^* + S_1 S_1^*) \quad (1.20)$$

The solutions to  $S_1, S_2$  for small gold particles in a fluid were published in 1908 by Gustav Mie (see [7]) and are discussed in subsection 1.1.6.

We now switch back to properties of scattering off of many particles. For a collection of identical particles, either a large enough collection of randomly oriented or any collection of spheres, scattering independently, it must hold

$$b_{\text{sca}} = n \cdot \sigma_{\text{sca}} \quad (1.21)$$

For unpolarized incident light, the total phase function is then also independent of the azimuthal angle  $\varphi$ , which is relevant because our nephelometers only measure the scattering along a single azimuthal angle and then multiply by  $2\pi$ .

### 1.1.6 Mie's Solution and Scattering in Different Regimes

Classification into different scattering regimes of scattering by a particle is done by introducing a measure for the relative size of the particle. Comparing the radius  $r$  of a particle to the wavelength  $\lambda$  of incoming radiation, one defines the *size parameter*  $x(r, \lambda)$  as

$$x(r, \lambda) = \frac{2\pi r}{\lambda} \quad (1.22)$$

Mie derived the general solution, including polarization, for plane waves scattering off of a spherically symmetric, homogeneous particle by expanding the solutions to Maxwell's equations in spherical harmonics[7]. He therefore also derived the solution to the phase function from Equation 1.20. The solutions however still contain infinite sums of coefficients that remain to be determined individually, which make it a task for computers and appropriate approximations as to when to terminate the sums. Directly citing from Hovenier et al.([3], p.45), these solutions for non-magnetic materials take the shape

$$S_3(\theta) \equiv S_4(\theta) \equiv 0 \quad (1.23)$$

$$S_1(\theta) = \sum_{n=1}^{\infty} \frac{2n+1}{n(n+1)} (a_n^* \pi_n(\cos \theta) + b_n^* \tau_n(\cos \theta)) \quad (1.24)$$

$$S_2(\theta) = \sum_{n=1}^{\infty} \frac{2n+1}{n(n+1)} (b_n^* \pi_n(\cos \theta) + a_n^* \tau_n(\cos \theta)) \quad (1.25)$$

where

$$\pi_n(\cos \theta) := \frac{d P_n(\cos \theta)}{d \cos \theta} \quad (1.26)$$

$$\tau_n(\cos \theta) := \cos \theta \pi_n(\cos \theta) - \sin^2 \theta \frac{d \pi_n(\cos \theta)}{d \cos \theta} \quad (1.27)$$

,  $P_n(\cos \theta)$  being the Legendre polynomial and  $a_n^*, b_n^*$  the so called *Mie coefficients*, which depend on the size parameter and the complex refractive index. Notice that other conventions exist, and for example Bohren and Huffman define  $\pi_n, \tau_n$  using *associated* Legendre polynomials[2].

### Rayleigh Scattering

In the case of  $r \ll \lambda$ , we can terminate the series after the first term, which is equal to approximating the particle as a dipole. Therefore the solution is valid for particles of arbitrary shapes in this regime[3]. We introduce the polarizability  $\alpha$ , which is related to the refractive index of the material. For isotropic  $\alpha$  the phase function is of the form[3]

$$F_{11}(\theta) = \frac{k^6 |\alpha|^2}{2} (1 + \cos^2(\theta)) \quad (1.28)$$

Consider now a collection of identical particles that are not necessarily of spherical symmetry (ie.  $\alpha$  not isotropic), but randomly oriented.

We want to provide yet another way of calculating the phase function in the Rayleigh regime, as we will use it in the experiment. Following Prahl, who in turn cites Bohren and Huffman, the scattering efficiency up to fourth order in size parameter is given by ([2], eq. 5.8)

$$Q_{\text{sca}}^{\text{ray}} = \frac{8}{3} x^4 \left| \frac{m^2 - 1}{m^2 + 2} \right|^2 \quad (1.29)$$

, where  $m$  is the complex refraction index of the material. For  $|m|x \ll 1$  it holds  $|b_1| \ll |a_1|$ [2]. We denote a phase function that is normalized such that an integration of the phase function over  $S^2$  yields  $Q_{\text{sca}}$  as  $p_{11}(\theta)$ , in mathematical terms

$$\int_{S^2} p_{11}(\theta, \phi) d\Omega = Q_{\text{sca}} \quad (1.30)$$

Using this normalization, we adapt Bohren and Huffman's equation 5.4 of the scattering matrix to third order in the size parameter  $x$  to be[2]

$$S_1 = \frac{1}{\pi x^2} \frac{3}{2} a_1(x, m) \quad (1.31)$$

$$S_2 = \frac{1}{\pi x^2} \frac{3}{2} a_1(x, m) \cos(\theta) \quad (1.32)$$

, where

$$a_1 = -\frac{2ix^3}{3} \frac{m^2 - 1}{m^2 + 2} \quad (1.33)$$

, which we can then insert in Equation 1.20 yielding  $p_{11}(\theta)$  (instead of  $F_{11}(\theta)$ ). If we obtain a phase function through Rayleigh scattering theory (i.e. Equation 1.31, Equation 1.33), we denote it as  $F_{11}^{\text{ray}}$ . The index *ray* indicates the method through which the phase function is obtained, not the size parameter of the particles considered.

### Mie Scattering

It is when  $r \sim d$ , that it makes sense to approximate Mie's exact solution by solving for the Mie coefficients. According to Bohren and Huffman, a rule of thumb is that about  $x$  terms in the expansion provide an accurate enough result[2]. If we obtain a phase function through Mie theory, we denote it as  $F_{11}^{\text{mie}}$ . We remark, that Mie theory also provides the correct results for Rayleigh scatterers and as for  $F_{11}^{\text{ray}}$ , the index *mie* indicates only the method through which the phase function is obtained, and is not related to the size parameter of the particles considered. For clarification we want to emphasize, that if in applications we did not terminate the calculation after a given number of terms in Equation 1.24, Equation 1.25, Mie scattering yielded the exact (i.e. theoretical) solutions.

### Geometric Scattering

When  $r \gg \lambda$ , we enter the geometrical scattering regime. We would then need many terms of the expansion to get a satisfying solution, and maybe a different ansatz than Mie theory is better suited. We do not enter the geometric regime with the particles investigated in this thesis.

## 1.2 Nephelometers

Nephelometers used in this context are integrating nephelometers, measuring the total or hemispherical back scattering coefficient of a sample, without considering the Rayleigh scattering at the carrier gas.

Air or other gases, possibly containing further aerosols such as dust, soot or any kind of vapor, are pumped into the nephelometer at a given flow rate. The device then illuminates the sample and measures how much of the total incoming intensity has been deflected. Such devices, adding up intensity from all angles, are called integrating nephelometers.

**Errors and uncertainty propagation** Because most of the measured values are the mean of an array, if not mentioned otherwise, I take the standard error of the mean (SEM) as its error. For a set  $\{x_i\}_{i=1}^n$  it is defined as the standard deviation (STD) divided by the sample size[13], so

$$\text{sem}(\{x_i\}_{i=1}^n) = \frac{\text{std}(\{x_i\}_{i=1}^n)}{\sqrt{n}} = \sqrt{\frac{\sum_{i=1}^n (x_i - \bar{x})^2}{(n-1) \cdot n}} \quad (1.34)$$

where  $\bar{x}$  is the mean of the sample, defined as[13]

$$\bar{x} = \frac{\sum_{i=1}^n x_i}{n} \quad (1.35)$$

I propagate errors according to Gaussian error propagation, giving explicit theoretical expressions but using Lebigot's *uncertainties* package for coding. I do not assume errors in the individual measurements themselves, nor in any literature values. For example, I do not consider errors stemming from illuminating wavelength discrepancies due to finite bandwidth.

### 1.2.1 Nephelometer Calibration in the Rayleigh Regime and Relation between Theoretical and Measured Scattering Coefficients

We introduce the following nomenclature. *neph* indicates the type of nephelometer used (here NE300 or IN101, see chapter 2). *angwidth*, short for angular width, describes the range of polar angles included. It is of types full scattering *sca*, covering the range  $0^\circ$  to  $180^\circ$ , hemispherical forward scattering *fsca*, only including polar angles from  $0^\circ$  to  $90^\circ$ , or hemispherical back scattering *bsca*, integrating over polar angles from  $90^\circ$  to  $180^\circ$ .

The conversion from theoretical values at standard pressure (101 320 Pa) and standard temperature (273.2 K) is done according to[15]

$$b_{\text{angwidth}}^{\text{theo}}(T, P) = b_{\text{angwidth}}^{\text{theo, STP}} \frac{273.2}{T} \frac{P}{101320} \quad (1.36)$$

From the symmetry of a Rayleigh scatterers phase function it follows, that the theoretical values for hemispherical back scattering coefficients are half those of total scattering. In the Rayleigh regime, scattering coefficients for different wavelengths are inversely proportional to the fourth power of the wavelength[8]. This implies

$$b_{\text{angwidth}}^{\text{theo}}(\lambda) = b_{\text{angwidth}}^{\text{theo, } \lambda_{\text{ref}}} \cdot \left( \frac{\lambda_{\text{ref}}}{\lambda} \right)^4 \quad (1.37)$$

, where  $\lambda_{\text{ref}}$  is the illuminating wavelength at which the literature values (provided and motivated in subsection 2.1.2) are given. I assume both, the reference and nephelometer illuminating wavelength, to be exact.

Finally, calibrating the nephelometers in the Rayleigh regime, we require

$$b_{\text{angwidth}}^{\text{neph, Rayleigh, } \lambda} = b_{\text{angwidth}}^{\text{theo, Rayleigh}}(T, P, \lambda) \quad (1.38)$$

$$= b_{\text{angwidth}}^{\text{theo, Rayleigh, STP, } \lambda_{\text{ref}}} \cdot \frac{273.2}{T} \frac{P}{101320} \cdot \left( \frac{\lambda_{\text{ref}}}{\lambda} \right)^4 \quad (1.39)$$

For temperature and pressure we use the time average over the measurement period  $\langle T \rangle, \langle P \rangle$ , provided by the respective nephelometer. As errors we propagate their SEMs  $\text{sem}(T), \text{sem}(P)$ . Assuming correlation of temperature and pressure negligible, this yields a SEM of

$$\text{sem}\left(b_{\text{angwidth}}^{\text{neph, Rayleigh, } \lambda}\right) = b_{\text{angwidth}}^{\text{neph, Rayleigh, } \lambda} \cdot \sqrt{\left(\frac{\text{sem}(T)}{T}\right)^2 + \left(\frac{\text{sem}(P)}{P}\right)^2} \quad (1.40)$$

In 1996, Anderson et al. analyzed an integrating nephelometer of model 3563 produced by TSI Inc. Analyzing aerosols with scattering coefficients between 0.2 and 6 times the one of air at standard pressure and temperature, they found linear regression correlation coefficients of  $r^2 \geq 0.999$  in 22 out of 24 cases and  $r^2 \geq 0.990$

in the remaining two[16]. This leads us to assume the raw signal from the photomultiplier tube (PMT) to be linearly dependent on the scattering coefficient in the Rayleigh regime. For the IN101, having one detector measuring hemispherical forward and one measuring hemispherical back scattering (see section 2.1.2), the over a measurement period time averaged raw signal for full scattering is  $\langle s_{sca}^{\text{IN101}} \rangle = \langle s_{bsca}^{\text{IN101}} + s_{fbsca}^{\text{IN101}} \rangle$ . The mathematical expression capturing the linear dependence expected is then for both nephelometers

$$b_{\text{angwidth}}^{\text{neph}, \lambda} (\langle s_{\text{angwidth}}^{\text{neph}, \lambda} \rangle) = c_{0, \text{angwidth}}^{\text{neph}, \lambda} + c_{1, \text{angwidth}}^{\text{neph}, \lambda} \cdot \langle s_{\text{angwidth}}^{\text{neph}, \lambda} \rangle \quad (1.41)$$

where  $c_0$  is usually called *offset* and  $c_1$  is called *gain* or *span*.

When calibrating the nephelometers we define the values of offset  $c_{0, \text{angwidth}}^{\text{neph}, \lambda}$  and gain  $c_{1, \text{angwidth}}^{\text{neph}, \lambda}$  such that the scattering coefficients deducted using Equation 1.41 match the theoretical values of the Rayleigh scattering gases CO<sub>2</sub> and Air at given temperatures, pressure and wavelength obtained from Equation 1.38, minus the scattering coefficient of air. We deduct the scattering coefficient of air because the sample will be suspended in filtered air, adding additional scattering signal we have to compensate. Thus, we calibrate the nephelometers such that illuminating filtered air yields a zero scattering coefficient

$$0 = c_{0, \text{angwidth}}^{\text{neph}, \lambda} + c_{1, \text{angwidth}}^{\text{neph}, \lambda} \cdot \langle s_{\text{angwidth}}^{\text{neph}, \lambda, \text{air}} \rangle \quad (1.42)$$

and illuminating pure CO<sub>2</sub> yields a scattering coefficient of

$$b_{\text{angwidth}}^{\text{neph}, \lambda, \text{CO}_2} - b_{\text{angwidth}}^{\text{neph}, \lambda, \text{air}} = c_{0, \text{angwidth}}^{\text{neph}, \lambda} + c_{1, \text{angwidth}}^{\text{neph}, \lambda} \cdot \langle s_{\text{angwidth}}^{\text{neph}, \lambda, \text{CO}_2} \rangle \quad (1.43)$$

We get a system of two equations for each pair of offset and gain of the shape

$$\begin{pmatrix} 1 & \langle s_{\text{angwidth}}^{\text{neph}, \lambda, \text{air}} \rangle \\ 1 & \langle s_{\text{angwidth}}^{\text{neph}, \lambda, \text{CO}_2} \rangle \end{pmatrix} \cdot \begin{pmatrix} c_{0, \text{angwidth}}^{\text{neph}, \lambda} \\ c_{1, \text{angwidth}}^{\text{neph}, \lambda} \end{pmatrix} = \begin{pmatrix} 0 \\ b_{\text{angwidth}}^{\text{neph}, \lambda, \text{CO}_2} - b_{\text{angwidth}}^{\text{neph}, \lambda, \text{air}} \end{pmatrix} \quad (1.44)$$

The inverse of a non-singular two by two matrix  $A = \begin{pmatrix} a & b \\ c & d \end{pmatrix}$  is given by its adjoint divided by its determinant,  $A^{-1} = \frac{1}{\det A} \begin{pmatrix} d & -b \\ -c & a \end{pmatrix}$  (insert for proof). Thus, assuming  $\langle s_{\text{angwidth}}^{\text{neph}, \lambda, \text{air}} \rangle \neq \langle s_{\text{angwidth}}^{\text{neph}, \lambda, \text{CO}_2} \rangle$ , we conclude

$$\begin{pmatrix} c_{0, \text{angwidth}}^{\text{neph}, \lambda} \\ c_{1, \text{angwidth}}^{\text{neph}, \lambda} \end{pmatrix} = \frac{1}{\langle s^{\text{CO}_2} \rangle - \langle s^{\text{air}} \rangle} \begin{pmatrix} \langle s^{\text{CO}_2} \rangle & -\langle s^{\text{air}} \rangle \\ -1 & 1 \end{pmatrix} \cdot \begin{pmatrix} 0 \\ b^{\text{CO}_2} - b^{\text{air}} \end{pmatrix} \quad (1.45)$$

where I omitted the indices angwidth, neph, λ on the RHS for sake of legibility.

Assuming the errors to be uncorrelated, we get standard error of the

$$\begin{aligned} \text{sem}(c_0)^2 &= \left( \frac{\langle s^{\text{air}} \rangle}{\langle s^{\text{CO}_2} \rangle - \langle s^{\text{air}} \rangle} \right)^2 \cdot \text{sem}(b^{\text{air}})^2 + \left( -\frac{\langle s^{\text{air}} \rangle}{\langle s^{\text{CO}_2} \rangle - \langle s^{\text{air}} \rangle} \right)^2 \cdot \text{sem}(b^{\text{CO}_2})^2 \\ &\quad + \left( \frac{-(b^{\text{CO}_2} - b^{\text{air}})\langle s^{\text{CO}_2} \rangle}{(\langle s^{\text{CO}_2} \rangle - \langle s^{\text{air}} \rangle)^2} \right)^2 \cdot \text{sem}(s^{\text{air}})^2 + \left( \frac{(b^{\text{CO}_2} - b^{\text{air}})\langle s^{\text{air}} \rangle}{(\langle s^{\text{CO}_2} \rangle - \langle s^{\text{air}} \rangle)^2} \right)^2 \cdot \text{sem}(s^{\text{CO}_2})^2 \end{aligned} \quad (1.46)$$

and

$$\begin{aligned} \text{sem}(c_1)^2 &= \left( \frac{-1}{\langle s^{\text{CO}_2} \rangle - \langle s^{\text{air}} \rangle} \right)^2 \cdot \text{sem}(b^{\text{air}})^2 + \left( \frac{1}{\langle s^{\text{CO}_2} \rangle - \langle s^{\text{air}} \rangle} \right)^2 \cdot \text{sem}(b^{\text{CO}_2})^2 \\ &\quad + \left( \frac{b^{\text{CO}_2} - b^{\text{air}}}{(\langle s^{\text{CO}_2} \rangle - \langle s^{\text{air}} \rangle)^2} \right)^2 \cdot \text{sem}(s^{\text{air}})^2 + \left( -\frac{b^{\text{CO}_2} - b^{\text{air}}}{(\langle s^{\text{CO}_2} \rangle - \langle s^{\text{air}} \rangle)^2} \right)^2 \cdot \text{sem}(s^{\text{CO}_2})^2 \end{aligned} \quad (1.47)$$

for both nephelometers and all angular widths and illuminating wavelengths.

I want to remark, that many more intricate methods of calibration exist (see e.g. [16]). A next step in accuracy could be achieved by specifically describing noise, for example by subtracting dark counts or measuring wall scattering, although these are also accounted for in our method.

### 1.2.2 The Illumination Function

In order to constrain ourselves to for the experiment relevant theory, we from now on assume our source to be unpolarized and the measured particles to be spheres or very small. Indeed, these assumptions are valid for in our experiment because LEDs emit unpolarized light, the calibration gases are in the Rayleigh regime (see subsection 1.1.6) and DEHS-aerosols are spherical (see subsection 2.2.1).

A perfect instrument would measure all polar angles  $\theta$  and do so with the same weight. However, due to physical constraints such as finite size, a real instrument can never achieve this. A nephelometer's unique weight function, the *angular illumination function*  $i_{\text{angwidth}}^{\text{neph}, \lambda}(\theta)$ , quantifies this, and without loss of generality differs for full and hemispherical back scattering as well as for different illuminating wavelengths. A perfect instruments illumination function is unity. In spherical coordinates, and assuming azimuthal invariance, the Jacobi determinant implies that unity corresponds to  $\sin \theta$ , and the measured scattering coefficients match the theoretical scattering coefficients. The samples theoretical scattering coefficient is denoted as  $b_{\text{sca}}^{\text{perf}}$ , where *perf* stands for the instrument being perfect. We use the following expressions of the different theoretical scattering coefficients

$$b_{\text{sca}}^{\text{perf}} = \int_{S^2} F_{11}(\theta) d\Omega = 2\pi \int_0^\pi F_{11}(\theta) \sin(\theta) d\theta \quad (1.48)$$

and similarly for hemispherical back scattering

$$b_{\text{bsca}}^{\text{perf}} = \int_{\{S^2 | z \leq 0\}} F_{11}(\theta) d\Omega = 2\pi \int_{\pi/2}^\pi F_{11}(\theta) \sin(\theta) d\theta \quad (1.49)$$

A real instrument's illumination function will therefore (hopefully) be of some shape reminding of a sine, and always cut off (truncated) at the measurement limits. While the NE300, measuring full scattering with a single detector, has a single illumination function even for full scattering, we obtain IN101's full scattering illumination function by adding the respective wavelength's hemispherical forward and back scattering illumination function, so

$$i_{\text{sca}}^{\text{neph}, \lambda}(\theta) = i_{\text{fscsa}}^{\text{neph}, \lambda}(\theta) + i_{\text{bsca}}^{\text{neph}, \lambda}(\theta) \quad (1.50)$$

If the only deviation stemmed from the nephelometer not illuminating perfectly, the scattering coefficients we expected the devices to measure were proportional as

$$b_{\text{sca}}^{\text{illum, mie}} \propto 2\pi \int_0^\pi F_{11}^{\text{mie}}(\theta) i_{\text{sca}}^{\text{neph}, \lambda}(\theta) d\theta \quad (1.51)$$

for full scattering and

$$b_{\text{bsca}}^{\text{illum, mie}} \propto 2\pi \int_{\pi/2}^\pi F_{11}^{\text{mie}}(\theta) i_{\text{bsca}}^{\text{neph}, \lambda}(\theta) d\theta \quad (1.52)$$

for hemispherical back scattering, the proportionality factor depending on the normalization of the illumination function. Here the index *mie* indicates, that the phase function is obtained from Mie theory.

However, remember that offset and gain are calibrated such as to best fit the behaviour of a Rayleigh scatterer because we define them by requiring the measured (i.e. calibrated) and literature scattering coefficients of the calibration gases to be equal (see Equation 1.38), compensating any systematical errors such as non-perfect illumination. We need an expression that corrects a measured scattering coefficient for samples scattering differently from a Rayleigh scatterer and the instrument being non-perfect, but at the same time considers that during calibration we already accounted for the instrument's illumination function in case of Rayleigh scatterers. For identical particles, we introduce the full scattering coefficients obtained using Rayleigh theory for a perfect instrument

$$b_{\text{sca}}^{\text{perf, ray}} = 2\pi \int_0^\pi F_{11}^{\text{ray}}(\theta) \sin(\theta) d\theta \quad (1.53)$$

and a nephelometer with non-perfect illumination

$$b_{\text{sca}}^{\text{illum, ray}} \propto 2\pi \int_0^\pi F_{11}^{\text{ray}}(\theta) i_{\text{sca}}^{\text{neph, } \lambda}(\theta) d\theta \quad (1.54)$$

and equivalent for hemispherical forward and back scattering. We then define a normalized phase function  $P_{11}(\theta)$ , such that for a single particle size

$$P_{11}(\theta) = \frac{F_{11}(\theta)}{b^{\text{perf}}} \quad (1.55)$$

We fulfill the above correction requirements by multiplying the scattering coefficients of a perfect instrument (1.48) and (1.49) by the correction factor

$$\frac{\int_0^\pi P_{11}^{\text{mie}}(\theta) i_{\text{angwidth}}^{\text{neph, } \lambda}(\theta) d\theta}{\int_0^\pi P_{11}^{\text{ray}}(\theta) i_{\text{angwidth}}^{\text{neph, } \lambda}(\theta) d\theta} \quad (1.56)$$

, obtaining the corrected scattering coefficients

$$b_{\text{angwidth}}^{\text{corr}} = b_{\text{angwidth}}^{\text{theo}} \cdot \frac{2\pi \int_0^\pi F_{11}^{\text{mie}}(\theta) i_{\text{angwidth}}^{\text{neph, } \lambda}(\theta) d\theta}{b_{\text{angwidth}}^{\text{perf, mie}}} \cdot \frac{b_{\text{angwidth}}^{\text{perf, ray}}}{2\pi \int_0^\pi F_{11}^{\text{ray}}(\theta) i_{\text{angwidth}}^{\text{neph, } \lambda}(\theta) d\theta} \quad (1.57)$$

where  $b_{\text{angwidth}}^{\text{theo}} = b_{\text{angwidth}}^{\text{perf, mie}}$ , because we assume Mie theory to provide exact results.

## 1.3 Particle Distributions

### 1.3.1 Normal Distribution

The normal or Gaussian distribution is a very common distribution in natural sciences, as for example the Binomial distribution and the Poisson distribution tend towards it for larger sample sizes and larger expectation values, respectively[17]. The probability distribution function (PDF) of a normal distribution is given by[17]

$$f(x) = \frac{1}{\sigma\sqrt{2\pi}} \exp\left(-\frac{(x-\mu)^2}{2\sigma^2}\right) \quad (1.58)$$

### 1.3.2 Lognormal Distribution

Consider some set of real numbers larger than zero. If taking its item wise logarithm yields a new set that is normally distributed, the original set followed a so called lognormal distribution. The PDF of a lognormal distribution is[18]

$$f_X(x) = \frac{1}{x \sigma\sqrt{2\pi}} \exp\left(-\frac{(\ln x - \mu)^2}{2\sigma^2}\right) \quad (1.59)$$

Its median is equal to its geometric mean, given by  $e^\mu$ [18].

If instruments measuring particle size use different bin widths, this results in different number concentrations for the same distributions[19]. As the bins are often logarithmically spaced, above potential error source can be eliminated by dividing by the difference in logarithms of bin borders[19], which infinitesimally corresponds to[19]

$$\frac{\Delta N_i}{\log_{10} D_{\text{upper},i} - \log_{10} D_{\text{lower},i}} \rightarrow \frac{dN}{d \log_{10} D_p} \quad (1.60)$$

where  $D_p$  is the midpoint diameter of the bin width.

We can relate this distribution to the diameter distribution by

$$\frac{dN}{d \log_{10} D_p} = \frac{dN}{dD_p} \frac{dD_p}{d \log_{10} D_p} \quad (1.61)$$

$$= \frac{dN}{dD_p} \left( \frac{d \log_{10} D_p}{dD_p} \right)^{-1} \quad (1.62)$$

$$= \frac{dN}{dD_p} \left( \frac{1}{D_p \ln(10)} \right)^{-1} \quad (1.63)$$

$$= \frac{dN}{dD_p} D_p \ln(10) \quad (1.64)$$

Combining both results, the corresponding PDF for a lognormal size distribution, measured in normalized bin widths, is given by

$$\frac{dN}{d \log D_p} = \frac{dN}{dD_p} D_p \ln(10) = \frac{\ln(10)}{\sigma \sqrt{2\pi}} \exp \left( -\frac{(\ln D_p - \mu)^2}{2 \sigma^2} \right) \quad (1.65)$$

It is this PDF that we fit the particle distributions to in subsection 3.3.2.

Now as to why we present the lognormal distribution. Different analyses have shown that natural distributions often exhibit a lognormal behavior[20], recent research has for example explored why droplets from water sprays follow lognormal distributions[21]. Generally, the aerosols created from a single source tend to follow a lognormal distribution[19].

### 1.3.3 Scattering Coefficients of Particle Distribution

Consider a set of particles with a diameter distribution  $n(D)$ , made up solely of one substance that is either spherically symmetric and nonmagnetic or randomly oriented and present in large enough numbers. Let the complex refractive index of the sample be  $m$ . The scattering coefficient of this distribution is then

$$b_{\text{sca}} = \int_{D_{\min}}^{D_{\max}} b_{\text{sca}}(n(D), x, m) dD \quad (1.66)$$

$$= \int_{D_{\min}}^{D_{\max}} n(D) \sigma_{\text{sca}}(x, m) dD \quad (1.67)$$

and similar for hemispherical back scattering. If the particles are described by a bin width normalized lognormal PDF  $n(D_p)$  with parameters  $\mu, \sigma$  and a total number concentration of  $N$  over all sizes, we conclude

$$b_{\text{angwidth}} = \int_{D_{p,\min}}^{D_{p,\max}} \frac{dN}{d \log D_p} \cdot b_{\text{angwidth}}(x, m) dD_p \quad (1.68)$$

$$= \int_{D_{p,\min}}^{D_{p,\max}} \frac{N \cdot \ln(10)}{\sigma \sqrt{2\pi}} \exp \left( -\frac{(\ln D_p - \mu)^2}{2 \sigma^2} \right) \cdot \sigma_{\text{angwidth}}(x, m) dD_p \quad (1.69)$$



# Chapter 2

## Methods

### 2.1 Work with Nephelometers

#### 2.1.1 Nephelometers Used and Their Mode of Operation

##### Aurora NE-300 Multi Wavelength Integrating Nephelometer

The Aurora NE-300 multi wavelength nephelometer, to which from this point onward we will refer as NE300, is an integrating nephelometer produced by Acoem Australasia that operates with three LED sources of wavelengths 635 nm, 525 nm and 450 nm within angles between  $7.3^\circ$  and  $172.7^\circ$ [4]. The used device has serial number 231689.

Hemispherical back scattering is automatically measured by covering parts of the light source emitting rays that make less than a  $90^\circ$  angle with the detector.

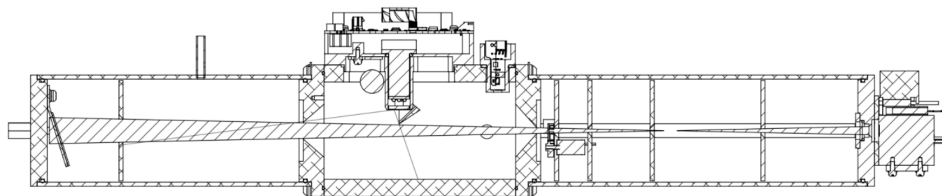


Figure 2.1: The light path of the NE300 nephelometer during hemispherical back scattering. Directly taken from the manual[4]

##### The Integrating Nephelometer IN101 by AirPhoton

The AirPhoton 3-wavelength Integrating Nephelometer IN101 is a relatively small and sturdy instrument. Operating LEDs at 632 nm, 532 nm and 450 nm[22], it applies a different measurement technique compared to the NE300.

The IN101 has two detectors, one covering hemispherical front scattering of angles between  $7^\circ$  and  $90^\circ$  and one covering hemispherical back scattering of angles between  $90^\circ$  and  $170^\circ$ [22]. The used device has serial number IN1064.

Hemispherical back scattering is then measured by only counting using the detector covering the larger angles, and it is not possible to make any further angular refinements.

### 2.1.2 Instrument Calibration

In order to determine offset and span from Equation 1.41 for each instrument and wavelength, the two Rayleigh scatterers CO<sub>2</sub> and air are used. Here *air* refers to ambient air filtered by a high efficiency particulate air (HEPA) filter, such that I can assume the remainder of small particles to be negligible. When measuring the properties of other aerosols suspended in air, the scattering coefficient of air has to be subtracted in order to solely measure scattering by the given sample. For this reason, the offset at a given wavelength is defined to be equal to the scattering coefficient of air at that wavelength.

Following the argument of Moallemi[23], we use the values provided by Dolgos and Martins for  $b_{\text{sca}}^{\text{theo,STP}}$  because they use instruments with similar wavelengths, which are  $b_{\text{sca}}^{\text{theo,STP, air}} = 14.02 \text{ Mm}^{-1}$  and  $b_{\text{sca}}^{\text{theo,STP, CO}_2} = 36.47 \text{ Mm}^{-1}$ [23] at 532 nm.

We calibrate the nephelometers for two reasons. Firstly, to calculate the calibration coefficients to be able to convert the PMT signal to scattering coefficients and perform sanity checks in case we obtain unreasonable results. Secondly, the instruments have their own software calculating scattering coefficients, which also needs to be calibrated. It is those measurements, that we primarily rely on and use for our calculations, as we believe them to be more accurate. I was not able to access or uncover the exact formulas the nephelometers' software use, although they are probably somewhat similar to the ones described in section 1.2. However, in this project we want to assess the values reported by firmware, so our calibration coefficients will not be further used and since both nephelometers' scattering coefficients measured during calibration agree with literature values, I proceed as described.

#### Calibration of NE300

The NE300 is capable of adding all counts towards full scattering independently, and separately also gives the counts in the hemispherical back scattering range.

#### Calibration of IN101

Due to the IN101 having two detectors for front and back scattering, we add both counts when calibrating full scattering and only include the counts from the back detector when calibrating hemispherical back scattering, as described in subsection 1.2.1.

### 2.1.3 Illumination Functions of the Nephelometers

For both devices, angular signal data was provided to the Atmospheric Physics and Optics group by the manufacturer. Due to the different builds, the respective data has a different structure. The goal of this part of the experiment is to provide analytical functions describing the instruments illumination function. In retrospective this proves to be not worth the effort and it's simpler and similarly accurate to interpolate the relative signal, as I will discuss in chapter 4. The second method is also the one applied in section 2.2.

#### Illumination Function of NE300

The data describing NE300's signal as a function of angle, where each of the six sets is divided by its respective maximum signal, can be seen in chapter 3, subsection 3.2.1. For full scattering, we simply perform a polynomial fit, For hemispherical back scattering however, we additionally set the fits' negative values to zero, as well as the positive values for angles smaller than approximately 1 rad. This is because

the polynomial fits alone display oscillations around zero in these areas and we do not want to just fit higher and higher order polynomials.

### Illumination Function of IN101

The data provided for the IN101, again each of the six sets divided by their respective maximum signal, is shown in Figure 2.2.

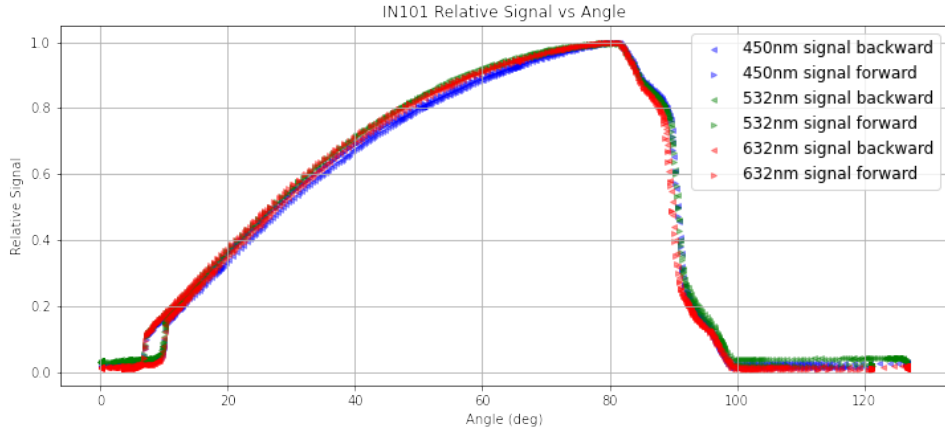


Figure 2.2: Relative signal vs. angle for the different wavelengths and detector regions (front scattering and back scattering) of IN101, provided by AirPhoton. Note that the angle is given as the difference from  $0^\circ$  for hemispherical front scattering and  $180^\circ$  for hemispherical back scattering.

Assessing the shapes in Figure 2.2, I decide to construct the final functions out of a combination of different functions. As not to overfit the data, I adjust initial guesses for forward and backward scattering but use the same functions.

At small angles, the data reminds us of an even monomial of high order. An ansatz is then

$$\text{func}_1(x, y_{\min}, b, c, d) := y_{\min} + bx + (c|x|)^d \quad (2.1)$$

where  $y_{\min}$  is the global minimum of the dataset, which, for unclear reasons, always occurs at small angles. The function contains both linear ( $b \cdot x$ ) and curved terms  $(c \cdot |x|)^d$ , allowing it to exhibit both linear and non-linear behavior. The curvature of the function is controlled by the parameters  $c$  and  $d$ . Higher values of  $c$  and  $d$  result in stronger curvature, while lower values lead to a flatter curve. The parameter  $y_{\min}$  acts as an offset, shifting the entire curve up or down and  $b$ ,  $c$ , and  $d$  control the scaling and shape of the curve. Physically this behaviour can be explained by the detector simply not being able to measure at these small angles, the measurement is truncated. Medium angles are exhibiting sine-like behaviour, which is good news when comparing to Equation 1.48 and Equation 1.49. We propose a sinusoidal curve with additional control over its behavior.

$$\text{func}_2(x, y_{\min}, e, f) := \max(\sin(ex - f), 3y_{\min}) \quad (2.2)$$

describes a squeezed or widened sine with a phase shift, as the observed roots of the data do not occur at zero. Taking the maximum of this curve and  $y_{\min}$  allows for a better combination of the three functions, but is not representing any characteristic of the values in these mid-range angles.

For a perfect instrument, the illumination function of one detector is a sine in the respective range and zero else, so zero for angles smaller/larger than  $\pi/2$  for front/back scattering. We can observe such a fall, but we observe symmetrical

deviations around the steep fall I cannot explain. Still, we make an ansatz using the following auxiliary equations. Let

$$\text{center} := \frac{\pi}{2} + g \quad (2.3)$$

$$y_{\tanh} = (\tanh((-x + \text{center})h) \cdot 0.5(1 - y_{\min})) + 0.5 + \frac{y_{\min}}{2} \quad (2.4)$$

$$y_{\text{gauss\_plus}} = A \exp\left(-\frac{(x - \text{center} - \text{centeroffset})^2}{\sigma}\right) \quad (2.5)$$

$$y_{\text{gauss\_minus}} = -A \exp\left(-\frac{(x - \text{center} + \text{centeroffset})^2}{\sigma}\right) \quad (2.6)$$

, then

$$\text{func}_3(x, y_{\min}, g, h, A, \sigma, \text{centeroffset}) := y_{\tanh} + y_{\text{gauss\_plus}} + y_{\text{gauss\_minus}} \quad (2.7)$$

This function combines a negative and shifted hyperbolic tangent with two Gaussian-like functions to further control the asymmetry. The parameters  $h$  and center control the steepness and center of the S-curve, respectively. Similar to  $\text{func}_1$ ,  $y_{\min}$  acts as an offset.  $A$  controls the overall scaling of the function. The parameters  $\sigma$  and centeroffset control the width and position of the Gaussian peaks, respectively. As depicted in Figure 2.3, the above functions were chosen such that the envelope the data, which itself is concave over large parts. We can then combine these functions describing the data partially to the following general ansatz, leaving away the input and parameters for sake of legibility.

$$f_{\text{tot}} := \max [\min(\text{func}_1, \text{func}_2, \text{func}_3), y_{\min}] \quad (2.8)$$

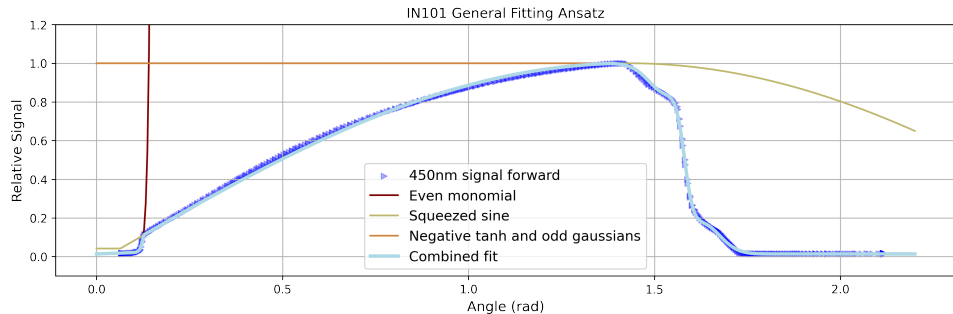


Figure 2.3: The combined ansatz for the illumination function of the IN101 with optimized parameters

We then solve for the optimal parameters using the *minimize* function from the *scipy.optimize* package.

## 2.2 DEHS Scattering

In subsection 2.1.2 we described how nephelometers are calibrated using air and CO<sub>2</sub>. With high enough angular resolution, for example provided by the NE300, one could reconstruct the phase function and then precisely calculate the scattering coefficient. However, nephelometers can not only report counts, but also directly calculate scattering coefficients. The fact that the calibration gases are Rayleigh scatterers (for which we can terminate the series expansion in Mie theory after first order, see subsection 1.1.6), could imply that the scattering coefficients reported

by the nephelometers are less accurate with larger size parameters of the analyzed aerosols. In this part of the experiment, we measure the scattering coefficients of different lognormal size distributions of DEHS using nephelometers IN101 and NE300 and compare the measurements to theoretical values of the same distributions obtained through Mie theory, as well as values obtained from our simple calibration according to Equation 1.41. Our goal is to gain an insight into the accuracy of the nephelometers' internal scattering coefficients calculation for aerosols in the Mie regime.

### 2.2.1 General Properties of DEHS

DEHS is a colorless, odorless and in water non-soluble substance that is often used to produce stable aerosols, for example when monitoring clean rooms[5]. Reasons are a long life time, low filter burden by sub micron particle sizes and, for this experiment most importantly, the aerosols being spherical[5]. The last fact makes Mie theory suitable to describe scattering by DEHS.

### 2.2.2 DEHS' Refractive Index

As one prerequisite of calculating scattering properties is knowledge of the, without loss of generality, complex refractive index, we need a model to describe it. From two different data sheets we take the literature values to be[5][6].

Wavelength (nm)	450	500	550	600	650
Refractive index	1.4585	1.4545	1.4535	1.4520	1.4500

Table 2.1: Literature values for the refractive index of DEHS at different wavelengths, obtained from [5][6]

Since the refractive index is about inversely proportional to the wavelength[25], we fit function

$$n(\lambda) = \frac{a}{\lambda} + b \quad (2.9)$$

to the theoretical values from Table 2.1 using *minimize* from *scipy.optimize*.

### 2.2.3 Experimental Setup

By pumping air through a *nebulizer* containing liquid DEHS at a flow rate of  $1 \text{ L} \cdot \text{min}^{-1}$  (liter per minute), we create an at this point unknown size distribution of (spherical) DEHS aerosols. To create a known and controlled charge distribution of the aerosols, which can be highly charged after creation[26], the particles are passed through a radioactive *neutralizer*, where the excess aerosol charge is conducted to the walls of the neutralizer, because the ions from radioactive decays create an electrically conductive environment[27]. Afterwards an *aerodynamic aerosol classifier* (AAC) selects a lognormal distribution around some chosen median. This is later verified by a *scanning mobility particle sizer* (SMPS). The AAC filters particles according to their aerodynamic diameter, a property describing how much an aerosol follows a medium flow[28]. As not to saturate the measurement devices that follow, we now dilute the size selected aerosols with  $10 \text{ L} \cdot \text{min}^{-1}$  of filtered air, regulating the flow via a *mass flow controller* (MFC). At this point we split the reduced concentration flow of  $11 \text{ L} \cdot \text{min}^{-1}$  of DEHS into five parts. To validate that the size selected aerosols indeed follow a lognormal distribution,  $0.3 \text{ L} \cdot \text{min}^{-1}$  are channeled into a SMPS, size selecting them in an electrostatic environment. Another  $0.3 \text{ L} \cdot \text{min}^{-1}$  are passed through a *condensation particle counter* (CPC), determining the number concentration of aerosols with an estimated accuracy of

10 % by condensating vapor upon them and optically analyzing the sample. Simultaneously, nephelometers NE300 and IN101 assess  $5.0 \text{ L} \cdot \text{min}^{-1}$  each, while the leftover flow remains unused.

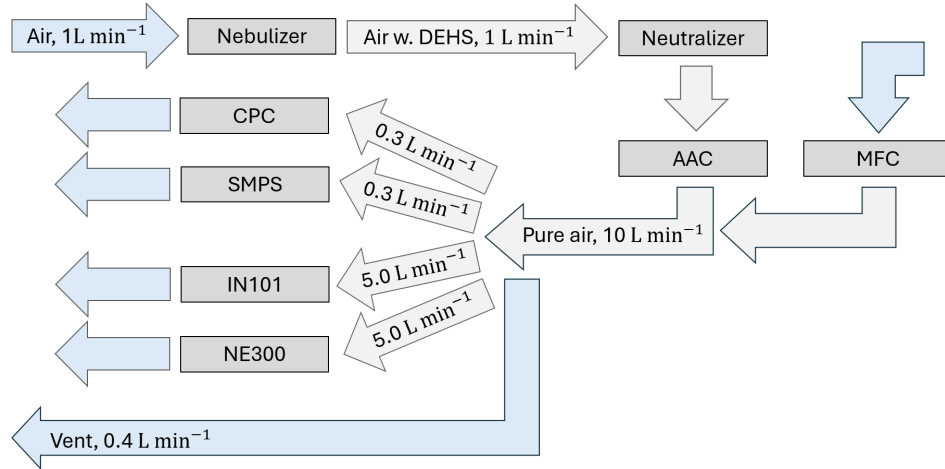


Figure 2.4: The setup for measuring the scattering coefficients of different lognormal size distributions of DEHS

#### 2.2.4 Calculation of Expected Scattering Coefficients

In order to obtain the corrected scattering coefficients of Equation 1.57 for a lognormal distribution of particles, we calculate corrected scattering cross sections which we then integrate over the particle sizes according to Equation 1.68. To obtain corrected scattering cross sections we use Equation 1.57, but normalise to scattering cross sections as the scattering coefficient is defined only for the entire collection. After adding the CPC's 10 % uncertainty, we compare the corrected values to

$$b_{\text{angwidth}}^{\text{meas}} = \langle b_{\text{angwidth}}^{\text{meas}} \rangle \pm \text{sem}(b_{\text{angwidth}}^{\text{meas}}) \quad (2.10)$$

. As we aim to test NE300 and IN101's firmware, we do not employ our calculated calibration coefficients to obtain measured scattering coefficients, using their reported values instead.

# Chapter 3

## Results and Discussion

### 3.1 Instrument Calibration

Adapting the theoretical scattering coefficients to recorded temperature and pressure (see Equation 1.36) and the nephelometers' wavelengths (see Equation 1.37) we solve the calibration equation (see Equation 1.45), yielding the calibration factors  $c_{0, \text{ang. width}}^{\text{neph}, \lambda}$ ,  $c_{1, \text{ang. width}}^{\text{neph}, \lambda}$  in Table 3.1, Table 3.2.

$\lambda$ (nm)	$c_{0,\text{sca}}^{\text{IN101}, \lambda} \times 10^{-2}$	$c_{1,\text{sca}}^{\text{IN101}, \lambda} \times 10^5$	$c_{0,\text{bsca}}^{\text{IN101}, \lambda} \times 10^{-1}$	$c_{1,\text{bsca}}^{\text{IN101}, \lambda} \times 10^5$
632	$-1.57 \pm 0.026$	$2.95 \pm 0.048$	$-7.84 \pm 0.13$	$1.47 \pm 0.024$
532	$-2.39 \pm 0.028$	$5.39 \pm 0.062$	$-11.9 \pm 0.14$	$2.69 \pm 0.031$
450	$-1.72 \pm 0.016$	$3.00 \pm 0.028$	$-8.60 \pm 0.081$	$1.50 \pm 0.014$

Table 3.1: Calibration coefficients  $c_{0, \text{ang. width}}^{\text{IN100}, \lambda}$ ,  $c_{1, \text{ang. width}}^{\text{IN100}, \lambda}$  for IN101

The back scattering offset values of IN101 are in the same order of magnitude as in the calibration instructions. The gains differ by 8 to 9 orders of magnitude, due to AirPhoton using a different calibration procedure. Therefore a comparison is not possible. Because I directly combine forward and back counts, I can't compare these values. The uncertainties of IN101 are on average 0.68 % for the offset and 1.24 % for the gain, analyzing 200 datapoints during 50 min of calibration time.

$\lambda$ (nm)	$c_{0,\text{sca}}^{\text{NE300}, \lambda} \times 10^{-3}$	$c_{1,\text{sca}}^{\text{NE300}, \lambda} \times 10^4$	$c_{0,\text{bsca}}^{\text{NE300}, \lambda} \times 10^{-3}$	$c_{1,\text{bsca}}^{\text{NE300}, \lambda} \times 10^4$
635	$-2.29 \pm 0.11$	$9.31 \pm 0.64$	$-1.146 \pm 0.056$	$4.66 \pm 0.23$
525	$-8.33 \pm 0.50$	$37.6 \pm 2.3$	$-4.17 \pm 0.25$	$18.8 \pm 1.1$
450	$-17.5 \pm 1.2$	$90.0 \pm 6.4$	$-8.77 \pm 0.62$	$45.0 \pm 3.2$

Table 3.2: Calibration coefficients  $c_{0, \text{ang. width}}^{\text{NE300}, \lambda}$ ,  $c_{1, \text{ang. width}}^{\text{NE300}, \lambda}$  for NE300

We observe the gain to decrease for larger wavelengths for the NE300. The uncertainties of NE300 are on average 5.94 % for the offset and 6.33 % for the gain. For NE300 we took 220 valid data points during 50 min. All obtained calibration coefficients are checked to fulfill the requirements Equation 1.42 and Equation 1.43.

### 3.2 Illumination Functions of the Nephelometers

#### 3.2.1 Illumination Function of NE300

In Figure 3.1 we see all illumination functions of the NE300. The fits are performed as described in section 2.1.3 and converged without difficulties. For full scattering,

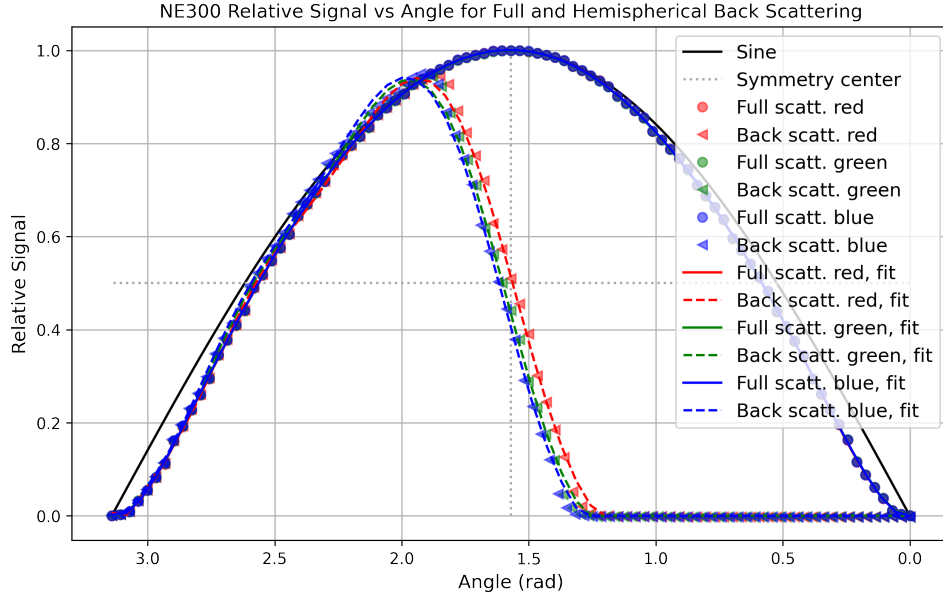


Figure 3.1: The relative signal and respective fits for the NE300, both full and hemispherical back scattering ranges are shown for NE300's wavelengths 635 nm (red), 525 nm (green) and 450 nm (blue). The axis orientation was chosen to be consistent with the angle conventions from Figure 1.3.

we observe that the data follows a sine more closely for angles closer to  $\pi/2$ , whereas symmetric deviations exist farther outwards. Regarding hemispherical back scattering, the signals that would ideally describe a perfect cut are of an approximately sigmoidal shape around, with longer wavelengths being more symmetric around the symmetry center ( $x = \pi/2, y = 0.5$ ). Separate illumination functions for the different illuminating wavelengths are plotted in subsection A.1.1.

### 3.2.2 Illumination Function of IN101

Scattering Type	bw blue	bw green	bw red	fw blue	fw green	fw red
Sum of residuals $\times 10^2$	2.40	2.91	3.05	2.86	3.06	3.87
Ratio to fw blue	0.84	1.02	1.07	1.00	1.07	1.35

Table 3.3: Minimized sum of least squares residuals and respective ratio to blue (450 nm) forward scattering. 'bw' stands for hemispherical back scattering and 'fw' stands for hemispherical forward scattering.

Due to IN101's build, where two separate detectors measure photons travelling to the front hemisphere ( $0 < \theta < \pi/2$ ) and to the back hemisphere ( $\pi/2 < \theta < \pi$ ), we additionally introduce *hemispherical forward scattering*. Having defined our fitting functions upon analyzing IN101's relative signal of 450 nm hemispherical forward scattering, we compare the ratios of the other fits in Table 3.3, to analyze whether our ansatz is suitable for all of IN101's data or only for 450 nm hemispherical forward scattering. The ratios are all within 1.35, hemispherical back scattering even having a better fit. I conclude, that the fitting ansatz is suitable for all wavelengths and also forward scattering. The optimized of the illumination function parameters for the different wavelengths and forward and back scattering are shown in Table 3.4.

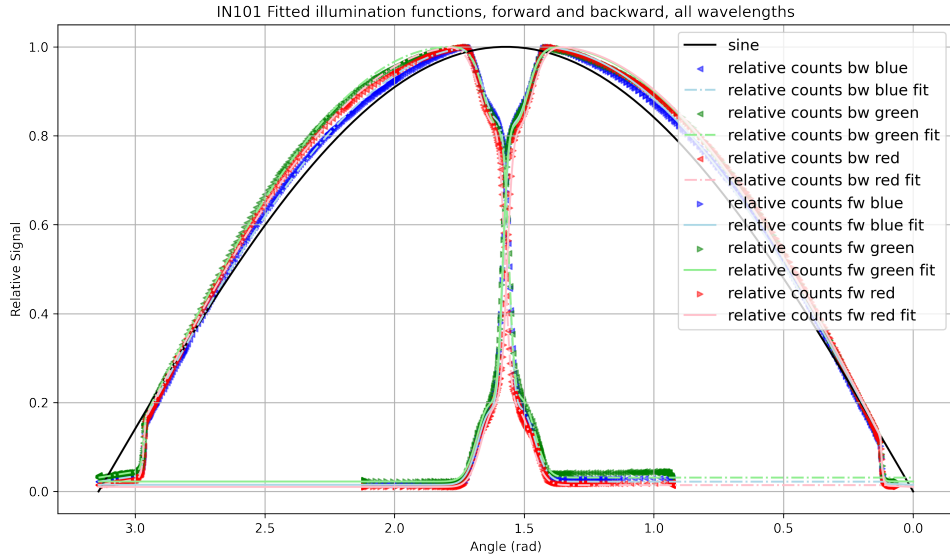


Figure 3.2: The relative signal and respective fits for the IN101, both full and hemispherical back scattering ranges are shown for IN101's wavelengths 632 nm (red), 532 nm (green) and 450 nm (blue). As in Figure 3.1, I choose to mirror the x-axis, such that the measurements of the back scattering detector ( $\triangleleft$ , left part of the plot) and front scattering detector ( $\triangleright$ , right part of the plot) match the coordinate conventions from Figure 1.3.

	bw blue	bw green	bw red	fw blue	fw green	fw red
$y_{\min} \times 10^2$	2.207	3.118	1.426	1.507	2.235	1.023
$b \times 10^2$	8.672	9.150	8.840	2.357	6.290	2.572
$c \times 10^0$	5.186	5.160	5.145	7.133	7.143	7.252
$d \times 10^{-1}$	2.763	2.480	2.468	2.157	2.124	2.235
$e \times 10^0$	1.090	1.189	1.151	1.099	1.139	1.147
$f \times 10^2$	3.230	4.485	4.140	1.490	1.767	1.941
$g \times 10^2$	1.226	1.232	-2.348	1.072	1.221	-4.475
$h \times 10^{-1}$	4.087	3.961	3.627	4.012	4.033	3.688
$A \times 10^1$	1.968	2.161	1.888	1.907	2.019	2.014
$\sigma \times 10^3$	5.418	5.410	5.555	5.041	5.182	5.250
centeroffset $\times 10^2$	3.919	3.833	4.291	4.044	4.047	4.075

Table 3.4: The different scattering types' optimized parameters for our model of IN101's illumination function (see Equation 2.8)

### 3.3 DEHS Scattering

#### 3.3.1 Refractive Index of DEHS

Fitting the inversely proportional function of Equation 2.9 to the literature values of DEHS' refractive index yields optimized parameters  $a = 11.53$ ,  $b = 1.432$ . Interestingly, this model reduces the minimized least square error by more than 40 %, compared to a linear fit ( $1.33 \times 10^{-6}$ ,  $2.27 \times 10^{-6}$  respectively). However, the uncertainty in the refractive index is negligible and given that we only have 5 data points, we cannot make a clear distinction of what model fits better or provides clearly better results.

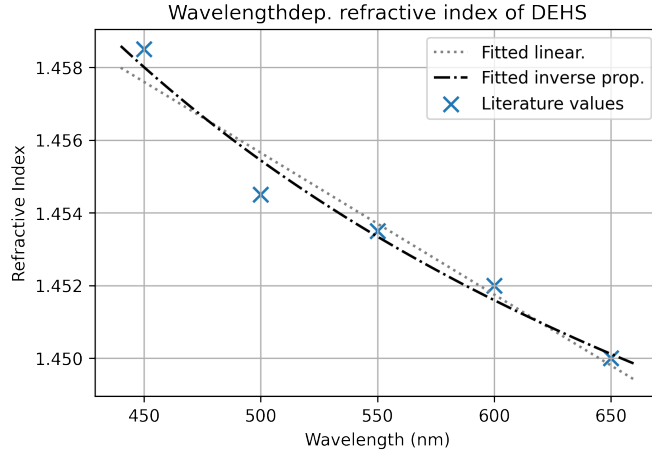


Figure 3.3: The literature values[5][6] of the refractive index of DEHS (compare Table 2.1) along with an inversely proportional fit (see Equation 2.9)

### 3.3.2 Particle Size Distribution

While measuring particles with a median diameter of about 300 nm and 600 nm, the CPC recorded an average number concentration of  $6106.9 \text{ cm}^{-3}$  and  $5962.3 \text{ cm}^{-3}$ , respectively. From the SMPS' measurements, I select three per median diameter that look the cleanest, disregarding others with for example multiple peaks. I then fit a lognormal distribution, normalized to bin width as discussed in subsection 1.3.2 and inserting an additional factor for number concentration which results in the distribution not being normalized anymore, to each size bin's mean value for both distributions. The result is plotted in Figure 3.4, yielding a geometric mean (=median) diameter of 313.5 nm and 594.7 nm and a geometric standard deviation of 1.16 and 1.07, respectively. However, the fitted number concentrations are  $7228.0 \text{ cm}^{-3}$  and  $7411.0 \text{ cm}^{-3}$ , deviating from the CPC's values that were used in the calculations in subsection 3.3.3.

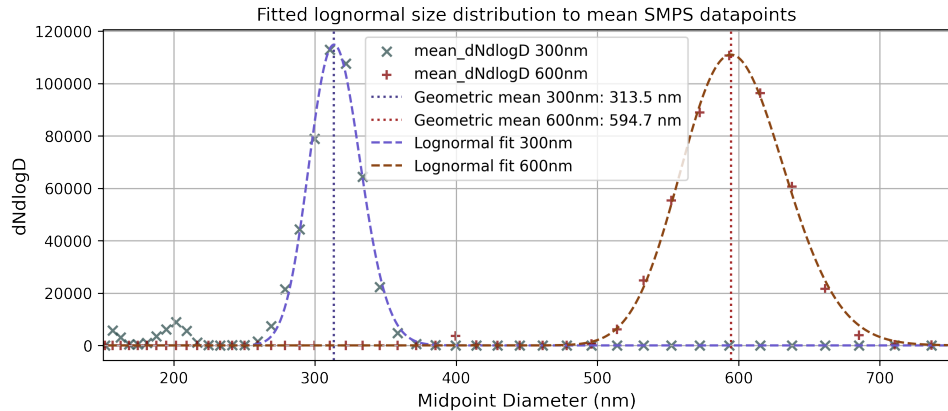


Figure 3.4: Scatter plot of mean midpoint diameter distributions for two particle size ranges, about 300 nm and about 600 nm. Additionally, a (not normalized) lognormal in spacing  $dN/d\log_{10} D_p$  fit is performed on each distribution, as described in Equation 1.65

### 3.3.3 Measured and Corrected Scattering Coefficients

In this section we compare the full scattering and hemispherical back scattering coefficients for two sizes of DEHS obtained from nephelometers NE300 and IN101 to the expected values, which are the values corrected according to Equation 1.57. To obtain the corrected scattering coefficients I use the SMPS's data fitted geometric mean and geometric standard deviation, as well as the number concentration measured by the CPC, for which I estimate an uncertainty of 10 %.

The measured and corrected scattering coefficients are presented in Table 3.5 and Table 3.6, where the row index is chosen to be applicable to both nephelometers, despite IN101/NE300 using the same illuminating wavelength 450 nm/450 nm for blue (B), but differing ones 532 nm/525 nm for green (G) and 632 nm/635 nm for red (R).

	$b^{\text{IN101, meas}}$	$b^{\text{IN101, corr}}$	$b^{\text{NE300, meas}}$	$b^{\text{NE300, corr}}$
full_B	$829.13 \pm 1.27$	$850.48 \pm 85.05$	$896.07 \pm 1.74$	$800.15 \pm 80.02$
full_G	$575.20 \pm 0.63$	$572.41 \pm 57.24$	$665.33 \pm 0.92$	$571.02 \pm 57.10$
full_R	$339.93 \pm 0.38$	$337.72 \pm 33.77$	$361.80 \pm 0.55$	$320.85 \pm 32.09$
back_B	$60.97 \pm 0.06$	$64.74 \pm 6.47$	$77.08 \pm 0.17$	$58.94 \pm 5.89$
back_G	$34.27 \pm 0.06$	$39.45 \pm 3.95$	$50.21 \pm 0.12$	$36.42 \pm 3.64$
back_R	$41.07 \pm 0.14$	$41.90 \pm 4.19$	$51.20 \pm 0.19$	$43.80 \pm 4.38$

Table 3.5: Measured and independent scattering coefficients adjusted for illumination function effect (i.e. expected scattering coefficients) ( $\text{Mm}^{-1}$ ) of the size distribution with a geometric mean of 313.5 nm. The expected values of IN101 and NE300 differ due to the different illuminating wavelengths and illumination functions of the nephelometers.

	$b^{\text{IN101, meas}}$	$b^{\text{IN101, corr}}$	$b^{\text{NE300, meas}}$	$b^{\text{NE300, corr}}$
full_B	$3246.35 \pm 3.06$	$6413.92 \pm 641.39$	$6191.99 \pm 25.68$	$5542.23 \pm 554.22$
full_G	$5610.25 \pm 8.40$	$5846.91 \pm 584.69$	$6274.02 \pm 28.79$	$5217.79 \pm 521.78$
full_R	$3280.45 \pm 2.03$	$4940.87 \pm 494.09$	$4983.98 \pm 22.42$	$4335.91 \pm 433.59$
back_B	$486.72 \pm 3.11$	$430.74 \pm 43.07$	$530.43 \pm 2.28$	$363.73 \pm 36.37$
back_G	$394.26 \pm 2.45$	$369.05 \pm 36.91$	$489.56 \pm 2.05$	$324.59 \pm 32.46$
back_R	$352.49 \pm 2.09$	$296.30 \pm 29.63$	$361.83 \pm 1.44$	$261.26 \pm 26.13$

Table 3.6: Measured and independent scattering coefficients adjusted for illumination function effect (i.e. expected scattering coefficients) ( $\text{Mm}^{-1}$ ) of the size distribution with a geometric mean of 594.7 nm. The expected values of IN101 and NE300 differ due to the different illuminating wavelengths and illumination functions of the nephelometers.

For the particle distribution with a geometric mean of 313.5 nm, the measured values of IN101 coincide with the corrected values when taking the uncertainties into account, except for green hemispherical back scattering, which deviates by  $1.17 \text{ Mm}^{-1}$ . All of NE300's measured values exceed the corrected values, deviating within 5.5 % for full scattering and 20.02 % for hemispherical back scattering.

We observe a different pattern for the particle distribution with a geometric mean of 594.7 nm. For both nephelometers' full and hemispherical back scattering, only IN101's green measured scattering coefficients match their respective expected value. For hemispherical back scattering, the values at least follow similar tendencies. After discussing with my advisors, I believe the IN101 to have been saturated for full scattering of the size distribution with a geometric mean of 594.7 nm, in other words the particle concentration being too high. A similar concentration saturating the

instrument for 600 nm particles, but providing the expected results for 300 nm particles is conceivable, since it is the scattered light and not the particle concentration that is decisive, despite of course the latter influencing the former.

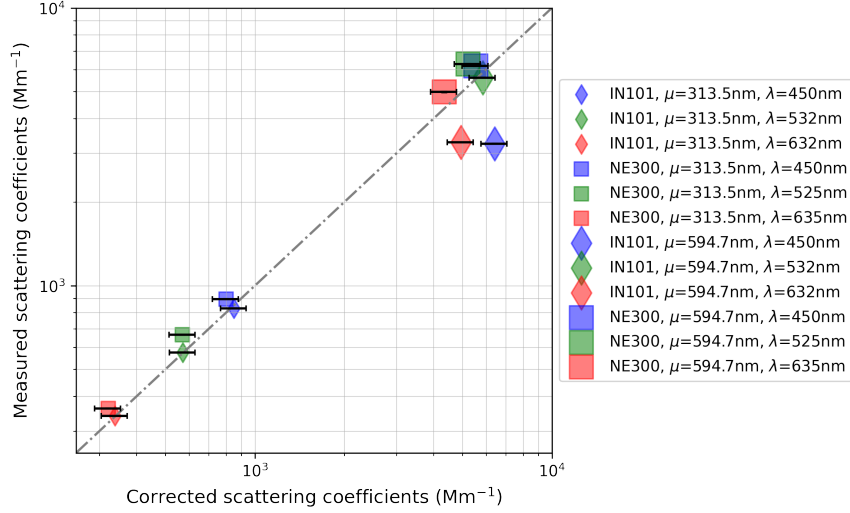


Figure 3.5: Measured versus corrected (independent scattering coefficients adjusted for illumination function effect) full scattering coefficients for both nephelometers. The data of IN101 of the size distribution with a geometric mean of 594.7 nm has been omitted due to saturation. The dashed line indicates the position of perfect agreement.

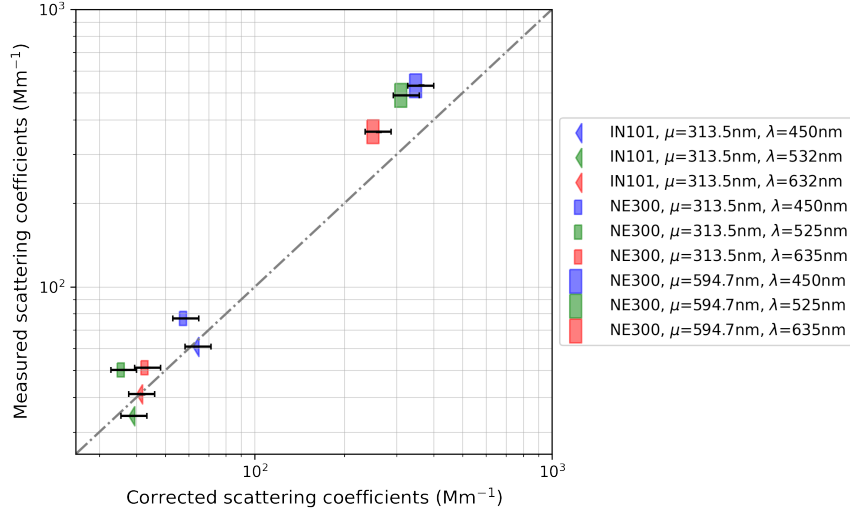


Figure 3.6: Measured versus corrected (independent scattering coefficients adjusted for illumination function effect) hemispherical back scattering coefficients for both nephelometers. The dashed line indicates the position of perfect agreement.

From the results of Table 3.5 and Table 3.6 (Figure 3.5, Figure 3.6), I present the calculated the hemispherical back scattering fraction  $\beta$  in Table 3.7 and Table 3.8. Notice that calculating  $\beta$  according to Equation 1.16 eliminates any influence of the number concentration, including the CPC's uncertainty. As this is the only uncertainty I consider when calculating the corrected scattering coefficients, also neglecting sizing uncertainty, I report the uncertainty in the corrected  $\beta$  to be integer zero.

	$\beta^{\text{IN101, meas}}$	$\beta^{\text{IN101, corr}}$	$\beta^{\text{NE300, meas}}$	$\beta^{\text{NE300, corr}}$
B	$0.074 \pm 0.000$	$0.076 \pm 0$	$0.086 \pm 0.000$	$0.074 \pm 0$
G	$0.060 \pm 0.000$	$0.069 \pm 0$	$0.075 \pm 0.000$	$0.064 \pm 0$
R	$0.121 \pm 0.000$	$0.124 \pm 0$	$0.142 \pm 0.001$	$0.137 \pm 0$

Table 3.7: Measured and expected hemispherical back scattering fraction  $\beta$  for the size distribution with a geometric mean of 313.5 nm

	$\beta^{\text{IN101, meas}}$	$\beta^{\text{IN101, corr}}$	$\beta^{\text{NE300, meas}}$	$\beta^{\text{NE300, corr}}$
B	saturated	$0.067 \pm 0$	$0.086 \pm 0.001$	$0.066 \pm 0$
G	saturated	$0.063 \pm 0$	$0.078 \pm 0.000$	$0.062 \pm 0$
R	saturated	$0.060 \pm 0$	$0.073 \pm 0.000$	$0.060 \pm 0$

Table 3.8: Measured and expected hemispherical back scattering fraction  $\beta$  for the size distribution with a geometric mean of 594.7 nm

To assess the nephelometers' internal consistency, we compare the measured and expected hemispherical back scattering ratio by dividing the former by the latter. Furthermore, we also investigate the spectral dependency of full scattering. Similar to the previous procedure, for both nephelometers and median diameters we calculate the measured and expected ratios of red full scattering divided by blue full scattering, green full scattering divided by blue full scattering and red full scattering divided by green full scattering. We then again take the ratio of measured and expected (i.e. independent scattering coefficients adjusted for illumination function effect) values.

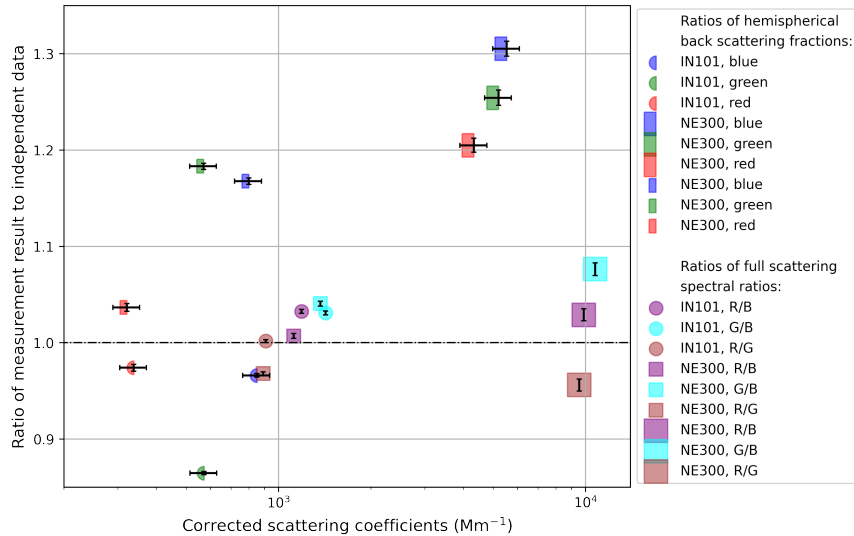


Figure 3.7: Ratios of measured to independent (i.e. expected, so corrected for illumination function and calibration: Firstly hemispherical back scattering ratios and secondly spectral ratios of full scattering coefficients. The smaller markers are indicating a geometric mean size of 313.5 nm, the larger ones a geometric mean size of 797.4 nm. The colors of the back scattering fractions correspond to the illuminating wavelength of the respective nephelometer. The x coordinate of a given ratio of full scattering spectral ratios is chosen as the mean corrected scattering coefficient of the two illuminating wavelengths of the respective colors.

Both results are presented in Figure 3.7, but ratios involving IN101's measurements of full scattering of the size distribution with a geometric mean of 594.7 nm are omitted, due to them being saturated. With the exception of red at the size distribution with a geometric mean of 313.5 nm, all ratios of hemispheric back scattering fractions deviate from unity by more than 10 %, the error bars being close to negligible. This indicates an instrument malfunction, an invalid illumination function, some other error source that remains to be identified and classified or, despite sanity checks, an error in the calculations. The team of PSI's Aerosol Physics and Optics Group is advised to further look into this. The ratios checking for internal consistency of spectral dependence are all within 8.3 % of unity, including error bars. Both size distributions have a mean ratio within 2.0 % of unity, the size distribution with a geometric mean of 313.5 nm however being less spread out. We can see a clear pattern of NE300 at both size distributions underestimating the ratios R/B, overestimating the ratios G/B and being closest for R/B. IN101 always overestimates the ratios being closest to unity for R/G.

# Chapter 4

## Conclusion

The determined calibration coefficients have reasonable uncertainties in the case of IN101. NE300's, however, with an average of 6.14 %, are on the larger side. In future work one could approach this differently, for example by incorporating more intricate formulas and separately accounting for noise such as wall scattering and dark counts, further increasing the relative signal difference for air and CO<sub>2</sub> and also take more data points.

Regarding the illumination functions, I would invest less time in fitting, because for the rest of the project I interpolated the measured values of the illumination function instead of using the fits. However, for NE300, if I were to fit the illumination function again, I would use a model based on a linear combination of a sinusoidal curves, as this more accurately represents the physical situation. Regarding the different measured number concentrations by SMPS and CPC, the CPC is generally more reliable for number concentrations than the SMPS due to the additional uncertainty of charging probability. Also, from my advisors' experience the CPC provides reliable results for particle concentrations below 10 000 cm<sup>-3</sup>.

While IN101 was saturated for full scattering at the size distribution with a geometric mean of 594.7 nm, NE300 was never. IN101, at the point it provided data, was more accurate but generally underestimated scattering coefficients. In contrary, NE300 consistently overestimated scattering coefficients. For the size distribution with a smaller geometric mean, IN101 had measured ratios of hemispherical back scattering fractions closer to the expected value than NE300, which for both size distributions produced hemispherical back scattering fractions far from the expected values. I believe the origin of this fact to be the most urgent to investigate in any future efforts, as also IN101 did not produce results one could generally be satisfied with (even at the single size it was not saturated). Both instruments performed well, significantly better than for hemispherical back scattering fraction, during test for spectral consistency. All values are within 8.2 % of unity, the values being even more accurate for the size distribution with a geometric mean of 313.5 nm.

The error ranges rarely cover a range for measured and expected values to overlap. Thus, a more detailed error analysis is needed and must be taken into account included in further assessments. Overall, for the analysis of the measuring accuracy of the nephelometers outside the Rayleigh regime, more trials with a larger variety of size distributions should be conducted. The NE300 seems to be more consistent at high concentrations and larger particles, but I cannot conclude if any or which of the two parameters is of prime relevance for nephelometer consistency and accuracy. It would be especially insightful to repeat all of the above measurements for multiple median diameters of size distributions and particle concentrations and vary the two parameters independently. This way, also the dominating influence on limits of nephelometer consistency and accuracy can be assessed.

# Bibliography

- [1] W. C. U. Dave3457, “File:linear polarization linearly polarized light plane wave.svg — wikimedia commons, the free media repository,” 2020, [https://commons.wikimedia.org/w/index.php?title=File:Linear\\_Polarization\\_Linearly\\_Polarized\\_Light\\_plane\\_wave.svg&oldid=513693092](https://commons.wikimedia.org/w/index.php?title=File:Linear_Polarization_Linearly_Polarized_Light_plane_wave.svg&oldid=513693092), accessed May 2, 2024, Image released to public domain.
- [2] C. F. Bohren and D. R. Huffman, *Absorption and Scattering of Light by Small Particles*. Wiley-VCH Verlag GmbH & Co. KGaA, 1983.
- [3] J. W. Hovenier, M. van der Mee, and H. Domke, *Transfer of Polarized Light in Planetary Atmospheres: Basic Concepts and Practical Methods*. Kluwer Academic Publishers, 2005.
- [4] Acoem Australasia, *Aurora NE Series User Manual 1.2*, 1st ed., December 15 2022, manual Revision History: Initial Release for Certification.
- [5] DEHA Haan & Wittmer GmbH, “Sicherheitsdatenblatt für dehs (di-ethyl-hexyl-sebacat) (auszug),” available from DEHA Haan & Wittmer GmbH, [www.deha-gmbh.de](http://www.deha-gmbh.de), accessed May 13, 2024.
- [6] Topas GmbH, “Di-ethyl-hexyl-sebacat (dehs): Safety data sheet,” June 2008, available from Topas GmbH, [www.topas-gmbh.de](http://www.topas-gmbh.de), accessed March 15, 2024.
- [7] G. Mie, “Beiträge zur Optik trüber Medien, speziell kolloidaler Metallösungen,” *Annalen der Physik*, vol. 330, no. 3, pp. 377–445, Jan. 1908.
- [8] J. E. Hansen and L. D. Travis, “Light scattering in planetary atmospheres,” *Space Science Reviews*, vol. 16, pp. 527–610, 1974, all Rights Reserved.
- [9] G. Graf, “Theoretische physik,” Lecture Notes, ETH Zurich, 2015, <https://edu.itp.phys.ethz.ch/15FS/tp/tp.pdf>.
- [10] H. Horvath, M. Kasahara, S. Tohno, F. Olmo, H. Lyamani, L. Alados-Arboledas, A. Quirantes, and V. Cachorro, “Relationship between fraction of backscattered light and asymmetry parameter,” *Journal of Aerosol Science*, vol. 91, pp. 43–53, 2016.
- [11] D. H. Staelin, “Boundary conditions for electromagnetic fields,” jun 16 2022, accessed May 15, 2024.
- [12] S. Prahl, “miepython,” <https://miepython.readthedocs.io/en/latest/index.html>, 2017–2024, accessed May 14, 2024.
- [13] J. I. Dong Kyu Lee and S. Lee, “Standard deviation and standard error of the mean,” *Korean Journal of Anesthesiology*, vol. 68, no. 3, pp. 220–223, Jun. 2015, published online 2015 May 28.

- [14] E. O. Lebigot, "Uncertainties: a python package for calculations with uncertainties," <http://pythonhosted.org/uncertainties/>, website accessed May 20, 2024.
- [15] T. L. Anderson and J. A. Ogren, "Determining aerosol radiative properties using the tsi 3563 integrating nephelometer," *Aerosol Science and Technology*, vol. 29, no. 1, pp. 57–69, 1998.
- [16] T. Anderson, D. Covert, S. Marshall, M. Laucks, R. Charlson, A. Waggoner, J. Ogren, R. Caldow, R. Holm, F. Quant, G. Sem, A. Wiedensohler, N. Ahlquist, and T. Bates, "Performance characteristics of a high-sensitivity, three-wavelength, total scatter/backscatter nephelometer," *Journal of Atmospheric and Oceanic Technology*, vol. 13, no. 5, pp. 967 – 986, 1996.
- [17] W. R. Leo, *Techniques for Nuclear and Particle Physics Experiments - A How-to Approach*, 2nd ed. Springer-Verlag Berlin Heidelberg GmbH, 1994, ISBN 978-3-540-57280-0.
- [18] S. Selvin, *The Log-Normal Distribution*. Cambridge University Press, 2015, p. 278–286.
- [19] "Aerosol statistics: Lognormal distributions and dn/dlogdp," U.S.A., 2012, <http://www.tsi.com>, accessed: May 13, 2024.
- [20] O. G. Raabe, "Particle size analysis utilizing grouped data and the log-normal distribution," *Journal of Aerosol Science*, vol. 2, no. 3, pp. 289–303, 1971.
- [21] M. R. O. Panão, "Why drop size distributions in sprays fit the lognormal," *Physics of Fluids*, vol. 35, no. 1, p. 011701, 01 2023.
- [22] Air Photon, "Airphoton 3-wavelength integrating nephelometers datasheet," [https://www.airphoton.com/uploads/7/6/0/6/76064899/airphoton\\_nepehlometers.pdf](https://www.airphoton.com/uploads/7/6/0/6/76064899/airphoton_nepehlometers.pdf), accessed May 6, 2024.
- [23] A. Moallemi, "Theoretical assessment, laboratory development, and field application of in situ aerosol characterization techniques based on ultra violet light induced fluorescence and multi-angle aerosol polarimetry," Doctoral Thesis, ETH Zurich, Zurich, 2022.
- [24] G. Dolgos and J. V. Martins, "Polarized imaging nephelometer for in situ airborne measurements of aerosol light scattering," *Optics Express*, vol. 22, no. 18, pp. 21 972–21 990, 2014.
- [25] J.-L. Meyzonnnette, J. Mangin, and M. Cathelinaud, *Refractive Index of Optical Materials*, ser. Springer Handbooks. Springer, 2019, pp. 997–1045, available from HAL: hal-02405126.
- [26] D. W. Cooper and P. C. Reist, "Neutralizing charged aerosols with radioactive sources," *Journal of Colloid and Interface Science*, vol. 45, no. 1, pp. 17–26, Oct. 1973.
- [27] W. A. Hoppel and G. M. Frick, "Aerosol charge distributions produced by radioactive ionizers," Naval Research Laboratory, Washington, DC 20375-5000, NRL Laboratory Report NRL Report 9108, May 1988, accessed May 13, 2024.
- [28] Cambustion, "What is aerodynamic diameter?" <https://www.cambustion.com/knowledgebase/what-is-aerodynamic-diameter>, accessed May 13, 2024.



# Appendix A

## Figures

### A.1 Illumination Functions

#### A.1.1 Illumination Functions of NE300

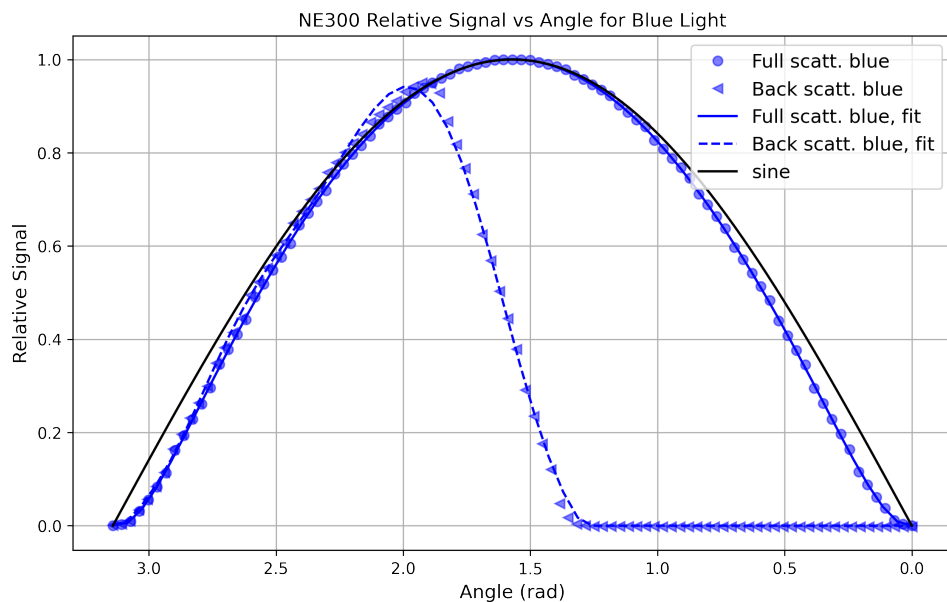


Figure A.1: NE300's full and hemispherical back scattering illumination function for an illuminating wavelength of 450 nm

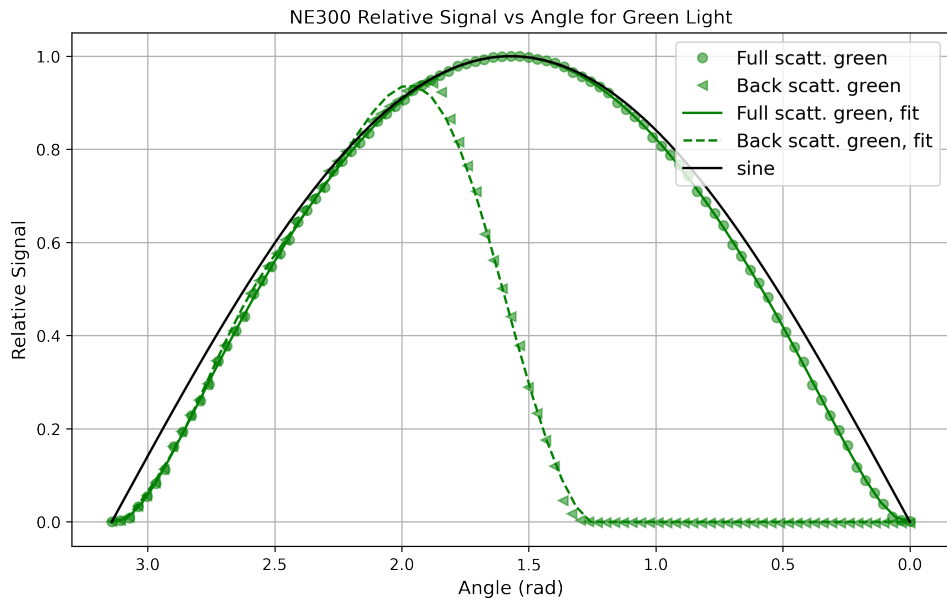


Figure A.2: NE300's full and hemispherical back scattering illumination function for an illuminating wavelength of 525 nm

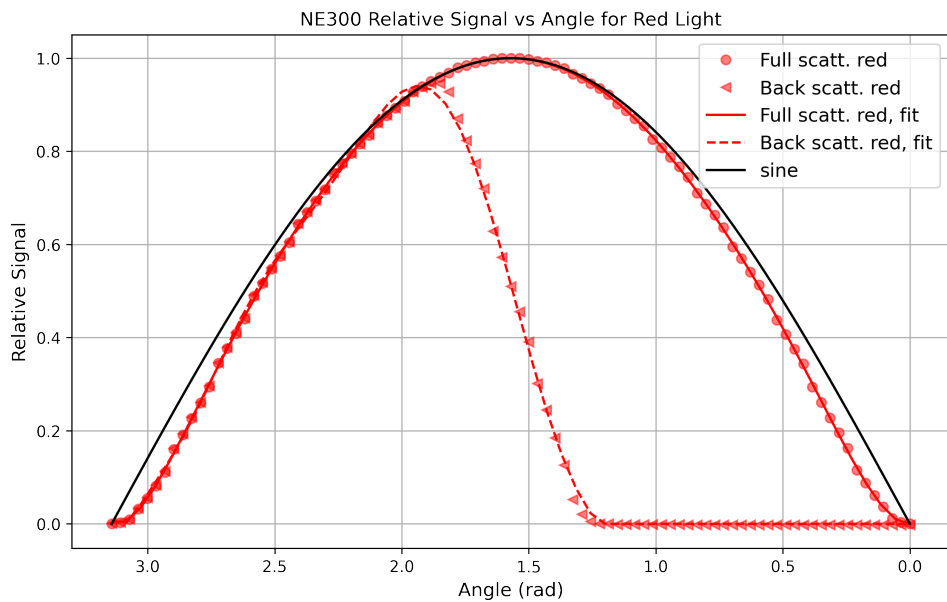


Figure A.3: NE300's full and hemispherical back scattering illumination function for an illuminating wavelength of 635 nm

### A.1.2 Illumination Functions of IN101

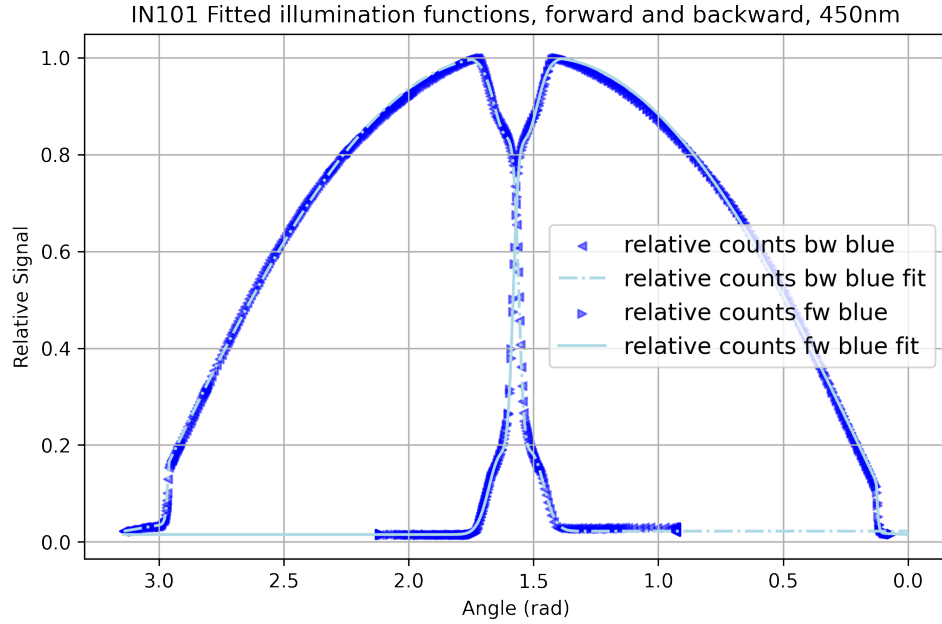


Figure A.4: IN101's full and hemispherical back scattering illumination function for an illuminating wavelength of 450 nm

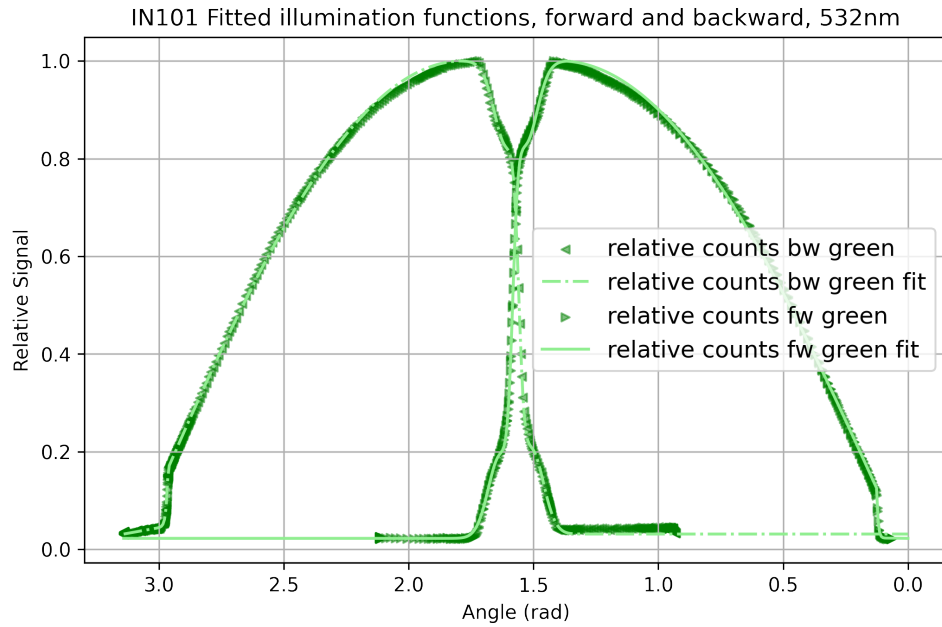


Figure A.5: IN101's full and hemispherical back scattering illumination function for an illuminating wavelength of 532 nm

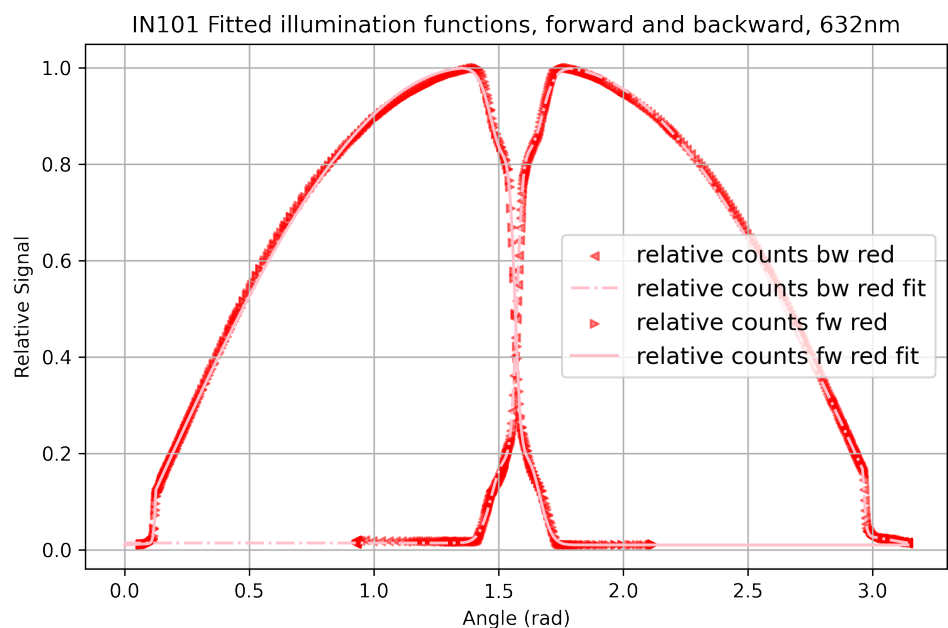


Figure A.6: IN101's full and hemispherical back scattering illumination function for an illuminating wavelength of 632 nm